博 士 論 文
(Doctoral Thesis)

Evolution of magnetic order in the frustrated quasikagome Kondo lattice $CeRh_{1-x}Pd_xSn$

(フラストレートした擬カゴメ近藤格子 $CeRh_{1-x}Pd_xSn$ における磁気秩序の発達)

杨 崇立

広島大学大学院先端物質科学研究科

(Graduate School of Advanced Sciences of Matter
Hiroshima University)

2018 年 9 月

(September 2018)

主　　査	准　教授	梅　尾　　和　則
審査委員	教　　授	鬼　丸　　孝　博
審査委員	教　　授	鈴　木　　孝　至
審査委員	特任教授	高　畠　　敏　郎

Table of Contents

(4) Superconductivity emerging from a suppressed large magnetoresistant state in tungsten ditelluride,
D. F. Kang, Y. Z. Zhou, W. Yi, C. L. Yang, J. Guo, Y. G. Shi, S. Zhang, Z. Wang, C. Zhang, S. Jiang, A. G. Li, K. Yang, Q. Wu, G. M. Zhang, L. L. Sun, and Z. X. Zhao,
Nature Communications **6**, 7804 /1-6 (2015).

(5) Quantum oscillations, thermoelectric coefficients, and the Fermi surface of semimetallic WTe_2,
Z. W. Zhu, X. Lin, J. Liu, B. Fauqué, Q. Tao, C. L. Yang, Y. G. Shi, and K. Behnia,
Physical Review Letters **114**, 176601 /1-5 (2015).

(6) Raman scattering investigation of large positive magnetoresistance material WTe_2,
W. D. Kong, S. F. Wu, P. Richard, C. S. Lian, J. T. Wang, C. L. Yang, Y. G. Shi, and H. Ding,
Applied Physics Letters **106**, 081906 /1-4 (2015).

(7) Large and anisotropic linear magnetoresistance in bulk stoichiometric Cd_3As_2 crystals,
D. S. Wu, X. Wang, X. Zhang, C. L. Yang, P. Zheng, P. G. Li, and Y. G. Shi,
Science China Physics, Mechanics and Astronomy **58**, 017501 /1-6 (2015).

(8) Effect of hydrostatic pressure on the superconducting properties of quasi-1D superconductor $K_2Cr_3As_3$,
J. P. Sun, Y. Y. Jiao, C. L. Yang, W. Wu, C. J. Yi, B. S. Wang, Y. G. Shi, J. L. Luo, Y. Uwatoko, and J. G. Cheng,
Journal of Physics: Condensed Matter **29**, 455603 /1-7 (2017).

Main Thesis

Abstract

1. Background and purpose

In rare-earth compounds, a quantum phase transition at zero temperature occurs between a magnetically ordered state and a paramagnetic one by passing through a quantum critical point (QCP). The QCP in 4*f* electron systems can be reached by tuning the balance between the on-site Kondo effect and the intersite Ruderman-Kittel-Kasuya-Yosida (RKKY) interaction by adjusting chemical composition, pressure, and magnetic field. Recently, an additional tuning parameter *Q*, magnetic frustration, was introduced to describe the unconventional quantum criticality in metallic 4*f* compounds. The magnetic frustration induced by geometrical frustration has been studied in antiferromagnets with a triangular lattice. It can't be satisfied that all the three spins can be antiparallel due to the antiferromagnetic (AFM) interaction. In these systems, highly correlated spin fluctuation down to zero temperature leads to the formation of a spin liquid state in which the spins are highly entangled with each other and simultaneously point in many directions. A Kondo lattice of Ce and Yb atoms with the kagome like geometry is expected to have an unconventional QCP, which is caused by the interplay among Kondo effect, RKKY-interaction, and magnetic frustration. A long-range AFM order can be induced from the spin liquid state by either destruction of the symmetry of frustrated structure or the breakdown of Kondo screening.

In addition to the geometrical origin, the correlated electron systems with well separated one-dimensional spin chains are expected to exhibit the magnetic frustration driven by a delicate balance between *n*-th nearest neighbor interactions along the chain. In the relevant Yb-based intermetallics, anomalous low-temperature phenomena have been suggested to be related to the chain-like configuration of the Yb ions. Therefore, the ground state of metallic Ce-based compounds with one-dimensional Ce chains deserves to be explored.

In order to study the quantum criticality in geometrically frustrated Kondo lattice compounds and the low-temperature properties of one-dimensional compounds, we have chosen Ce-based compounds, CeRhSn and $CePd_3Sn_2$, respectively. CeRhSn crystallizes in the hexagonal ZrNiAl-type structure with a quasikagome lattice of Ce atoms in the basal *c* plane. The Ce atom has nearest neighbors of four Rh2 atoms out of the plane. The strong hybridization

between the Ce 4*f* state and the 4*d* band from Rh2 atoms leads to a high Kondo temperature T_K ~ 200 K. A zero-field quantum critical point has been suggested by divergences in the specific heat coefficient C/T, magnetic susceptibility χ, and magnetic Grüneisen parameter. The anisotropic thermal expansion displays the critical behavior only along the *a* axis. The spin-flop crossover in the field dependence of C/T was observed near the magnetic field of $B \parallel a$ = 3.5 T. These experimental facts suggested that CeRhSn is located very close to a QCP due to the geometrical frustration.

By the present PhD work, a new ternary stannide $CePd_3Sn_2$ has been discovered. It is found to crystallize in the orthorhombic structure with one-dimensional chains of the shortest Ce-Ce distance along the *b* axis. In a few antiferromagnets with one-dimensional Ce chains, short-range correlations in the Ce chain have been claimed. For example, in an orthorhombic compound $CePt_5Ge_3$, AFM short-range correlations manifest themselves as a pronounced tail in the $C(T)$ above the three-dimensional long-range ordering temperature T_N = 1.1 K. On the contrary, $CePd_3In_2$ which is isostructural with $CePd_3Sn_2$ orders antiferromagnetically at T_N = 2.1 K where the magnetic entropy S_m is less than 0.8Rln2. The reduction of S_m from Rln2 was attributed to the Kondo effect with T_K ~ 2 K. An aluminide $CePd_3Al_2$ also shows an extended tail in C/T prior to the AFM order at T_N = 1.1 K, which was regarded as the result of the enhanced Kondo effect with T_K ~ 5.5 K.

The present work is aimed to clarify whether or not the quantum critical behavior in CeRhSn is driven by the geometrical frustration in the quasikagome lattice. For this purpose, we have substituted Pd for Rh and conducted measurements of magnetic, transport, and specific heat down to 0.03 K. In the substituted system $CeRh_{1-x}Pd_xSn$, a magnetic order is expected to be induced by the destruction of local symmetry of the frustrated lattice and/or the suppression of hybridization between the 4*f* orbitals and Rh 4*d* orbitals due to the additional 4*d* electron.

Another purpose of this work is to study the effect of short-range correlations in the systems with a chain of Ce atoms. For this purpose, we focus on a new compound $CePd_3Sn_2$. We have determined its crystal structure from single crystal x-ray diffraction and conducted the measurements of transport, magnetic, and thermal properties.

2. Quantum criticality and development of AFM order in $CeRh_{1-x}Pd_xSn$ with a quasikagome Ce lattice

In order to study how the frustrated ground state of CeRhSn is changed with substitution of

Pd for Rh, we have prepared samples of $CeRh_{1-x}Pd_xSn$ and measured the electrical resistivity ρ, magnetization M, magnetic susceptibilities χ_{dc} and χ_{ac}, and specific heat C. Polycrystalline samples of $CeRh_{1-x}Pd_xSn$ were prepared by the arc-melting method. With the increase in x from 0 to 0.75, the hexagonal a parameter linearly increases while the c parameter deviates from the Vegard's law. The polycrystalline samples are composed of grains preferentially oriented along the c axis. Along this direction, the electric current I and magnetic field B were applied in the measurements of resistivity and magnetization, respectively.

With Pd substitution, the change in the 4*f* state from a delocalized state to a localized one manifests itself in $\chi(T)$ and isothermal $M(B)$. For $x = 0$, the large and negative value of paramagnetic Curie temperature θ_p and the small effective magnetic moment μ_{eff} are characteristics of a valence fluctuating Ce compound. For $x \geq 0.65$, μ_{eff} increases nearly to the value for a free Ce^{+3} ion. For $x = 0.75$, $\chi(T)$ exhibits a peak at 3 K, suggesting an AFM order. The AFM order is corroborated by a spin-flop like behaviour in $M(B)$, which reaches a saturated value of 1.4 μ_B/Ce at 5 T. Emergence of a magnetic order in $CeRh_{1-x}Pd_xSn$ for $x = 0.1$ has been observed in temperature dependence of C/T. It exhibits $-\log T$ dependence which is followed by a maximum at 0.1 K. As x increases from 0.2 to 0.4, the temperature at the maximum of C/T gradually increases to 0.7 K. It is noteworthy that the maximum temperature for each x agrees with the maximum temperature of $\chi_{ac}(T)$. The magnetic entropy $S(T)$ curves for $x = 0.65$ and 0.75 are saturated to $R\ln 2$ at 10 K, confirming the doublet ground state of the localized 4*f* state under the crystal field.

For studying the emergence of AFM order for $x = 0.1$ in more detail, single crystals with $x = 0$ and 0.1 were prepared by the Czochralski method. Crystals oriented along the a and c axes were used for the measurements of temperature- and magnetic-field dependences of $\chi_{dc}(T, B)$, $\chi_{ac}(T, B)$, and electrical resistivity $\rho(T, B)$. The data of $\chi_{ac}(T)$ with $x = 0.1$ shows a maximum at 0.15 K, close to the temperature at maximum in $C(T)$. The field dependence of $\chi_{ac}(B \parallel a)$ for $x = 0$ exhibits a metamagnetic crossover at 3.5 T in agreement with the field dependence of C/T, which indicates the destruction of frustration among Ce moments in the c plane. For $x = 0.1$, the large anisotropy of $\rho(T)$, $\rho(I \parallel a) >> \rho(I \parallel c)$, is maintained. Both $\rho(I \parallel a)$ and $\rho(I \parallel c)$ show a continuous increase, which is attributed to the loss of coherent scattering. The large anisotropy $\chi_c(T) >> \chi_a(T)$ for $x = 0$ is maintained for $x = 0.1$. The positive magnetoresistance (MR) for $x = 0$ is the characteristic of coherent Kondo lattice compounds. On the contrary, MRs for $x = 0.1$ are all negative, which is the behavior of incoherent Kondo

lattice. The absolute value for $I \parallel B \parallel c$ at 8 T is approximately 5 times larger than that for $I \parallel B \parallel a$, which is consistent with that of $M(B \parallel c) \cong 5M(B \parallel a)$. The magnetic and transport properties for the single crystal with $x = 0.1$ show that the magnetic frustration and Kondo effect for $x = 0$ are both suppressed. As a result, an AFM order is induced at $x = 0.1$, leaving the quantum critical point at $x = 0$.

3. Antiferromagnetic short-range correlations in $CePd_3Sn_2$ with one-dimensional Ce chains

A new ternary stannide $CePd_3Sn_2$ has been discovered in the present work. Single crystal x-ray diffraction analysis revealed that it crystallizes in the orthorhombic structure with one-dimensional Ce chains running along the b axis. The measurements of C, χ, M, and ρ on polycrystalline samples were performed to explore the ground state properties of $CePd_3Sn_2$.

The $\rho(T)$ data show a metallic behavior with an obvious drop at 0.6 K, indicating a magnetic phase transition. The magnetic contribution ρ_m does not exhibit any sign of Kondo scattering. A maximum in $\chi(T)$ at 0.6 K suggests an AFM order. The isothermal magnetization $M(B)$ at 0.5 K bends at around 4 T and reaches 1.2 μ_B/Ce at 10 T. A sharp peak at 0.6 K in $C(T)$ agrees with that of the peak in $d\rho/dT$. Because no Kondo effect was observed in ρ_m(T), we attribute the tail from 0.6 K up to 3 K in $C(T)$ to AFM short-range correlations inherent in one-dimensional systems.

Contents

Chapter 1

Introduction

1.1 4*f*-electron systems

In the periodic table, the lanthanides from Ce (Z = 58) to Lu (Z = 71), where Z represents the atomic number, have the 4*f* shell. The 4*f* shell is occupied by up to fourteen electrons by following the Hund rule. In the case of partially filled 4*f* shell, the coupling between the total angular momentum L and the total spin momentum S provides the total momentum $J = |L \pm S|$, leading to a magnetic moment $\mu = g_J [J (J + 1)]^{1/2}$. Therefore, the 4*f* electrons are responsible for the magnetic properties of rare-earth compounds. The 4*f* electrons are well localized due to the deep distribution of 4*f* electrons wave function inside the closed 5*s* and 5*p* shells [1], as shown in the Fig. 1.1. In Ce-based intermetallic compounds, however, the tail of the wave function of the 4*f* electron overlaps those of ligand electrons, leading to the hybridization between 4*f* electrons and conduction electrons.

In Ce-based intermetallic compounds, the exchange coupling between the localized 4*f* electron and conduction electrons governs the competition between the Kondo effect and the Ruderman-Kittel-Kasuya-Yosida (RKKY) interaction [2, 3, 4]. When the magnetic ordering is quenched by the Kondo effect, the system reaches a quantum critical point at zero temperature. For compound with Ce atoms in a geometrically frustrated lattice, we expect unconventional quantum criticality where a spin liquid state competes or cooperates with a Kondo singlet state [5, 6, 7, 8]

1.2 Quantum criticality

1.2.1 Kondo effect and RKKY interaction

Kondo effect

The electrical resistivity $\rho(T)$ of metals slightly doped with *d* or *f* electron elements usually exhibits a minimum followed by a continuous increase in proportional to $-\ln T$ [9, 10]. It is attributed to the scattering of conduction electrons by the exchange interaction with localized magnetic moments of isolated magnetic impurities. The mechanism of this phenomenon has been explained by the *s*-*d* exchange model described as

$$H = \sum_{k\sigma} \xi_k \, c^{\dagger}_{k\sigma} c_{k\sigma} + J\boldsymbol{S} \cdot \boldsymbol{s}_0, \tag{1.1}$$

where ξ_k is the kinetic energy of conduction electrons, $c^{\dagger}_{k\sigma}$ and $c_{k\sigma}$ are creation and annihilation operators for conduction electrons, J is the coupling between conduction electrons and localized moment, $\boldsymbol{S}$ is the localized spin of magnetic impurity, and $\boldsymbol{s}_0$ is the spin density of conduction electrons at the position of the impurity. On the scattering, the spin flip happens simultaneously for both the conduction electron and magnetic impurity. The calculation for its second order perturbation [11, 12] reveals the logarithmic temperature dependence of $\rho(T)$ as

$$\rho(T) = \rho_{\mathrm{B}} \left(1 + 2JD_{\mathrm{c}}(E_{\mathrm{F}}) \ln \frac{W}{k_{\mathrm{B}}T}\right), \tag{1.2}$$

where $D_{\mathrm{c}}(E_{\mathrm{F}})$ is the conduction electron density at the Fermi energy E_{F} and W is the band width. The minimum of $\rho(T)$ can be well explained by combining with the term from phonon scattering AT^5. On cooling, the localized moment is gradually screened by conduction electrons, then the Kondo singlet forms below the Kondo temperature

$$T_{\mathrm{K}} = \frac{W}{k_{\mathrm{B}}} \exp\left(-\frac{1}{JD_c(E_{\mathrm{F}})}\right). \tag{1.3}$$

RKKY interaction

In a Kondo lattice system [13], the magnetic ions such as Ce ions are periodically arranged in the lattice. At low temperatures, the intersite interaction of Kondo clouds become important. There is an indirect exchange interaction between localized moments mediated by conduction electrons, known as the RKKY interaction [13, 14, 15]. A localized magnetic moment polarizes the spins of conduction electrons and this polarization couples to anothor neighbouring localized magnetic moment. The RKKY interaction is described as

$$H = -\sum_{i,j} J(R_{ij})\boldsymbol{S}_i \cdot \boldsymbol{S}_j, \tag{1.4}$$

$$J(R_{ij}) \propto \frac{-2k_F R_{ij}\cos(2k_F R_{ij}) + \sin(2k_F R_{ij})}{(2k_F R_{ij})^4}, \tag{1.5}$$

where $J(R_{ij})$ expresses the interaction between the localized spins $\boldsymbol{S}_i$ and $\boldsymbol{S}_j$ at a distance R_{ij}. As shown in Fig. 1.2, the $J(R_{ij})$ has an oscillatory dependence from positive sign to negative one on R_{ij}, representing the ferromagnetic and antiferromagnetic interactions, respectively [1]. The characteristic temperature T_{RKKY} [16] is given by

$$T_{RKKY} \sim \frac{J^2}{k_B} D_c(E_F) \tag{1.6}$$

In a 4*f* electron system, the *c*-*f* exchange interaction [17] is express as

$$J_{cf} \propto \frac{<|V|^2>}{E_F - E_{4f}}, \tag{1.7}$$

where V is the hybridization matrix element and E_{4f} is the energy of the 4*f* level with respect to E_F.

Doniach phase diagram

In a Kondo lattice system, the Kondo interaction screens the localized moments by the spin polarization of conduction electrons, while the RKKY interaction stabilizes the long-range magnetic order among the localized moments. The two interactions exhibit different dependence on J. The competition between the two leads to various ground states described by the Doniach phase diagram [16], as shown in Fig. 1.3.

In the regime of small J, T_{RKKY} is smaller than T_K and a magnetic order is expected to occur, which usually is an AFM order. In the regime of large J, T_K exceeds T_{RKKY}, then a coherent Kondo state is constructed and the system behaves as a Fermi liquid [18, 19, 20, 21, 22]. At $J = J_c$, the system reaches a quantum critical point (QCP), exhibiting a non-Fermi-liquid (NFL) behavior [2, 3, 4, 23].

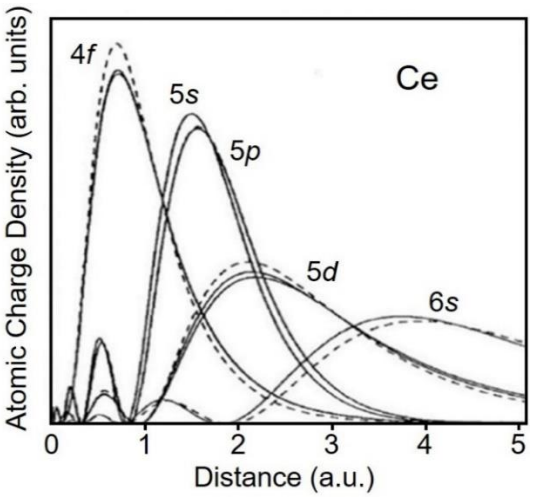

Figure 1.1: Radial distribution of atomic charge density for Ce [1].

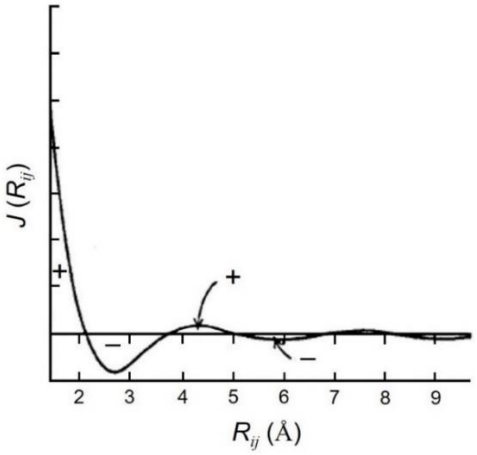

Figure 1.2: The indirect exchange interaction $J(R_{ij})$ as a function of the distance R_{ij} between the localized spins S_i and S_j [1].

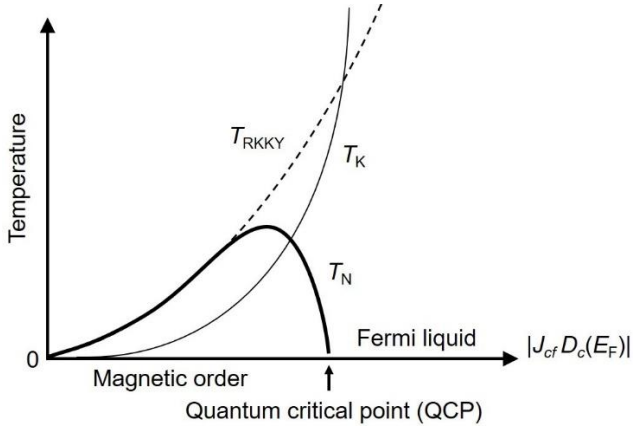

Figure 1.3: Doniach phase diagram for the Kondo lattice system [16]. The characteristic temperatures of Kondo effect and RKKY interaction, T_K and T_{RKKY}, are shown by dotted and broken lines, respectively. The antiferromagnetic temperature T_N is shown by the solid line.

1.2.2 Geometrical frustration and spin liquid

Geometrical frustration

In condensed matter physics, magnetic frustration arises from competing magnetic interactions among localized magnetic moments while can not be simultaneously satisfied. Such a phenomenon starts to be studied through antiferromagnets with geometrical origin. The classical example is a triangular spin lattice, where the nearest neighbors prefer to be anti-aligned, while three spins can not be all antiparallel. In an insulating system with a geometrically frustrated structure, spin-spin interactions act between the nearest and next nearest neighbors [24, 25]. In metallic systems, however, the interaction between localized moments is carried by conduction electrons. Therefore, the longer ranged interaction may make the magnetism partially frustrated [26, 27, 28]. On the other hand, the size of local magnetic moments in insulators is constant, while in metallic systems, the frustration can be suppressed and quenched with reducing the moments by the screening of conduction electrons. The geometrical frustration in metallic systems has been studied in the compounds with triangular [29, 30, 31, 32, 33], kagome [34, 35, 36, 37], Shastry-Sutherland [38, 39, 40, 41], and pyrochlore lattices [42, 43, 44, 45, 46]. As shown in Fig. 1.4, a $S = 1/2$ kagome two-dimensional lattice includes the nearest neighbor AFM interaction J_1 and the next nearest neighbor ferromagnetic (FM) coupling J_2 [6]. For example, Ce ions in a heavy-fermion antiferromagnet CePdAl form a quasikagome lattice. Only two thirds of Ce moments participate in a long-range AFM order and the other remain paramagnetic due to the geometrical frustration within the quasikagome lattice [47, 48]. On the checker-board array in a Sharstry-Sutherland lattice, the competition exists between the alternating diagonal AFM interaction J_1 and the nearest neighbor interaction J_2. The antiferromagnetic order is destroyed when the ratio J_1/J_2 is large [6]. In a three-dimensional pyrochlore lattice, the FM interaction between the nearest neighbors is frustrated due to the different Ising axes of the spins along local <111> axis [25].

Spin liquid

In geometrically frustrated magnets, the competing magnetic interactions lead to spin fluctuations. The degree of frustration in insulating systems is measured by a frustration parameter $f = |\theta_p|/T_c$ [25], where θ_p is the paramagnetic Curie-Weiss temperature and T_c is the temperature at which the spins order. For large size spins, at low temperatures, the fluctuation is driven by thermal energy and spins point to random directions with time. For small spins like $S = 1/2$, the zero-point motion in quantum mechanics maintains down to absolute zero

temperature. If the quantum fluctuations are coherent, a quantum spin liquid forms, whereby the spins are highly entangled with each other and simultaneously point to many directions.

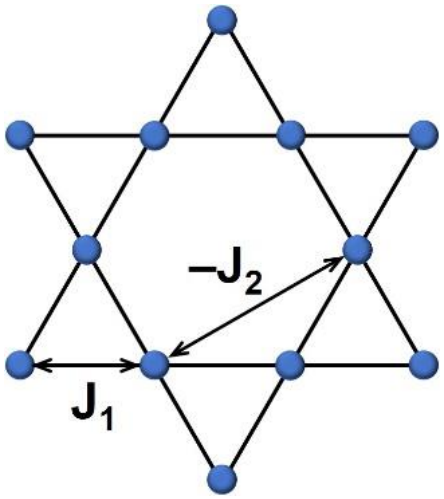

Figure 1.4: The geometrical frustrated $S = 1/2$ Kagome lattice with the nearest neighbor antiferromagnetic interaction J_1 and the next nearest neighbor ferromagnetic coupling J_2.

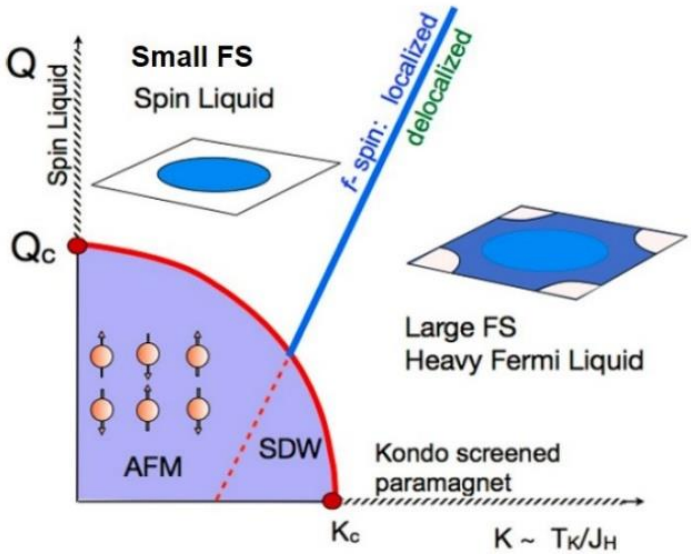

Figure 1.5: QK phase diagram of the frustrated Kondo lattice system constituted by Doniach axis $K \sim T_K/J^H$ and frustration axis Q. The spin liquid metal and heavy Fermi liquid are separated by a zero-temperature quantum phase transition [6].

QK diagram

Recently, an additional tuning parameter Q, which represents the quantum zero-point motion of spins induced by magnetic frustration, was introduced to describe the unconventional quantum criticality in the geometrically frustrated Kondo lattice. In this system, a spin liquid state competes with a Kondo singlet state due to the interplay among the RKKY-interaction, Kondo effect, and magnetic frustration. Hence, a long-range AFM order can be induced by either destruction of symmetry of frustrated structure or breakdown of Kondo screening. As shown in Fig. 1.5 [6], the horizontal axis is the Doniach axis $K \sim T_K/J^H$, where T_K is Kondo temperature and J^H represents the strength of RKKY interaction. The vertical axis is the frustration axis Q. The boundary of AFM phase is connected by two QCPs at Q_c and K_c. For large $K > K_c$ and small Q, the system reaches a heavy Fermi liquid state with a large Fermi surface. For small K and large $Q > Q_c$, however, the localized spins form a metallic spin liquid with a small Fermi surface.

1.2.3 Substitution effects and pressure effects on frustrated Kondo lattice compounds

A tuning parameter of the frustrated Kondo lattice systems is the parameter K, which is controlled by the *c-f* exhange interaction J_{cf}. Hence, adjusting the magnitude of *c-f* hybridyzation by substitution is one method to change among different ground states. For a quasikagome Kondo lattice CePdAl, which antiferromagnetically orders at 2.7 K, substituting an isovalent element Ni for Pd in $CePd_{1-x}Ni_xAl$ decreases the lattice parameter and thus enhances the *c-f* hybridyzation [49, 50, 51, 52, 53]. Thereby, the AFM order is completely suppressed at $x = 0.144$. The ratio $|\theta_p|/T_N$ increases with x as the Kondo effect surpasses the RKKY interaction. An opposite crossing of a QCP occurs in the isostructural alloy system $CeRh_{1-x}Pd_xIn$. With increasing x, a valence-fluctuating state in CeRhIn changes to an AFM heavy fermion state [54]. An AFM order appears only at a very high content $x = 0.8$ at $T_N = 0.65$ K, which rises to 1.7 K for $x = 1$. The crossing of the QCP is thought to be driven by the increase in the 4*d*-electron number. Thereby, the 4*f* level deepens from the Fermi level and thus weakens the hybridization between the Ce 4*f* state and Rh/Pd 4*d* states [54].

If application of pressure on the frustrated Kondo lattice could release the geometrical frustration without changing the Kondo coupling, the decrease in the tuning parameter Q may induce a long-range magnetic order or enhance the ordering temperature. For example, a heavy fermion antiferromagnet YbAgGe crystallizes in hexagonal ZrNiAl-type structure with a quasikagome lattice formed by Yb atoms in the *c* plane as shown in Fig. 1.6 [55, 56, 57]. Figure 1.7 shows the electrical resistivity ρ, magnetic susceptibility χ, and specific heat C, indicating two magnetic transitions at $T_{M1} = 0.8$ K (a second order) and $T_{M2} = 0.65$ K (a first order) [58]. The second-order magnetic transiton at T_{M1} is manifested in the decreases in ρ(I || a) and ρ(I || c), a broad anomaly in $\chi(T)$ in field B || a, and a peak in $C(T)$. The hysteresis behaviors in both ρ(I || a) and ρ(I || c) and a sudden drop in $\chi(T)$ in field B || a = 0.4 T suggest that the magnetic transition at T_{M2} is the first order. As shown in Fig. 1.8, the two magnetic transitons in $C(T)$ merge into one second-order transition at T_M at 1.6 GPa under hydrastatic pressure. As shown in Fig. 1.9, T_M and S_m both increase with increasing the pressure up to 3.22 GPa, while T_K keeps the constant value at 10 K. The origin of enhanced AFM order above 1.6 GPa is thought to be the release of magnetic frustration in the quasikagome lattice [59].

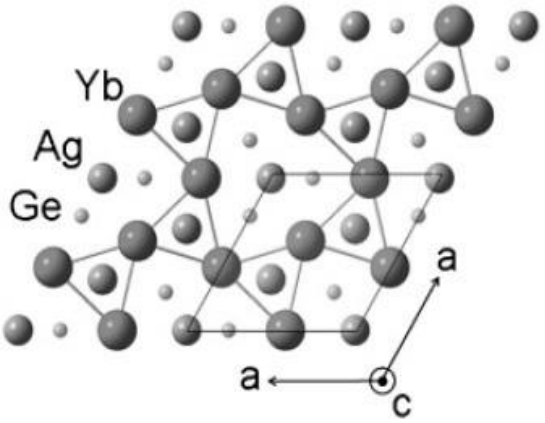

Figure 1.6: Crystal structure of YbAgGe along the hexagonal *c* axis. Yb atoms form a quasikagome lattice in the *c* plane [59].

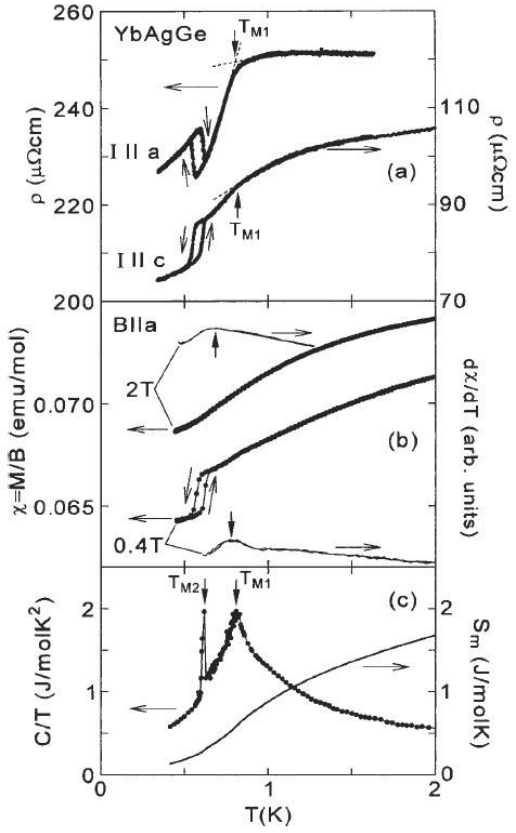

Figure 1.7: Temperature dependence of electrical resistivity $\rho(T)$, magnetic susceptibility $\chi(T)$, and specific heat $C(T)$ for YbAgGe. Vertical arrows indicate the magnetic ordering temperatures [58].

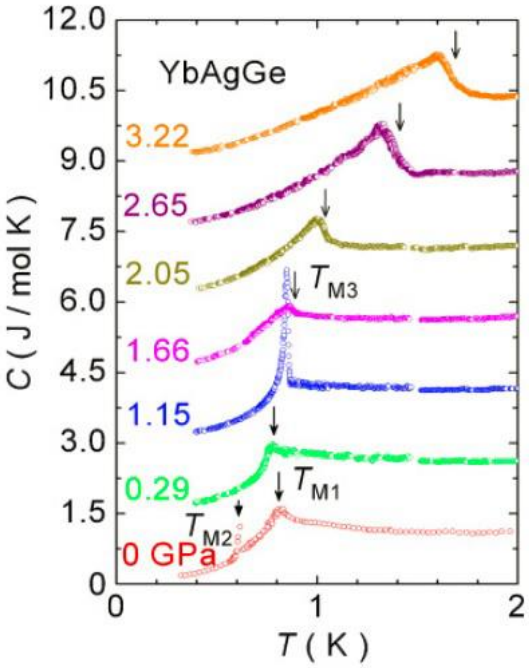

Figure 1.8: Temperature dependence of specific heat $C(T)$ of YbAgGe under hydrostatic pressure up to 3.22 GPa. Vertical arrows indicate the magnetic ordering temperatures [59].

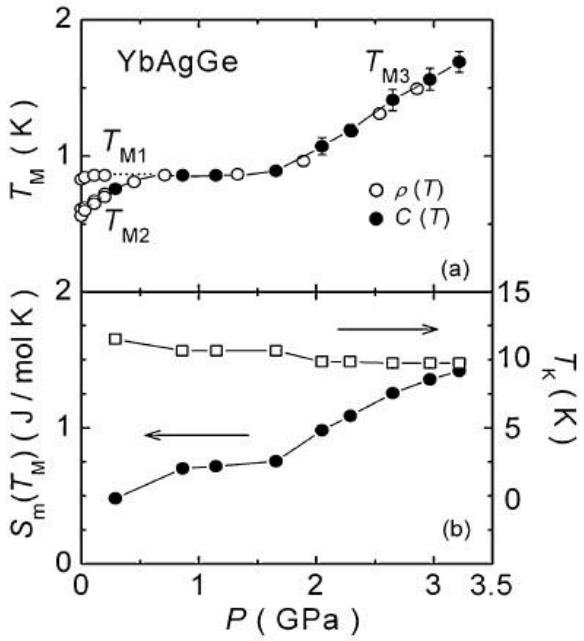

Figure 1.9: Pressure dependence of magnetic ordering temperature T_M, magnetic entropy S_m, and Kondo temperature T_K for YbAgGe [59].

1.2.4 Quantum criticality in the quasikagome Kondo lattice CePdAl

A well-studied heavy fermion antiferromagnet with a quasikagome lattice is CePdAl as shown in Fig. 1.10 [47, 48, 49, 60]. The nearly trivalent Ce ions occupy the 3*f* site in the hexagonal ZrNiAl-type structure with no inversion symmetry [61, 62]. The Ce ion has a localized Ising moment of 1.6 μ_B along the *c* axis. Below T_N = 2.7 K, a partially ordered magentic state was revealed by neutron diffraction measurements on powder samples [47]. Ce ions in the quasikagome lattice interact with the nearest neighbors by a FM interaction J_1 and with the next neighbors by an AFM interaction J_2. The FM chains formed by Ce (1) and Ce (3) are seperated by non-ordered Ce (2). Therefore, in single quasikagome layer, the two thirds of Ce moments participate in the long-range AFM order, the others remain paramagnetic. In three dimensional magnetic structure shown in Fig. 1.11, the 2D AFM ordered planes of Ce (1 and 3) are separated by the paramagnetic plane of Ce (2).

Based on the data of resistivity, ac susceptibility, and specific heat, a *T*-*B* phase diagram for CePdAl was constructed as shown in Fig. 1.12 [63, 64, 65]. With applying magnetic field along the Ising c axis, the AFM order in CePdAl is gradually suppressed. A sequence of metamagnetic transitions or crossovers appear between B || a = 3 and 5 T after which a paramagnetic phase is realized. In this phase, the magnetoresistance is negative, which is caused by the suppression of spin fluctuations arised from the geometrical frustration.

As mentioned in the last section, the substitution of Ni for Pd in CePdAl decreases the unit cell volume. Thereby, the *c*-*f* hybridization and Kondo effect are expected to be enhanced, leading to the suppression of AFM order. Actually, the specific heat data of $CePd_{1-x}Ni_xAl$ in Fig. 1.13 show that T_N decreases to zero at $x = 0.144$ and C/T is proportional to $-\log T$, exhibting the NFL behavior.

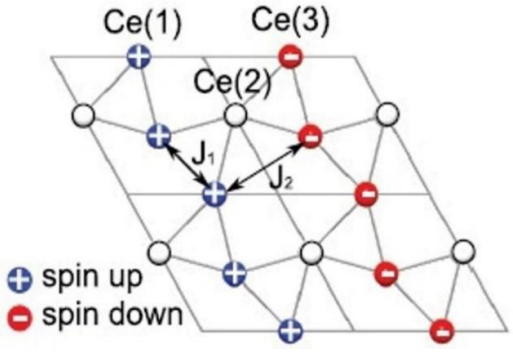

Figure 1.10: The two-dimensional magnetic structure of CePdAl in the *c* plane [49]. J_1 represents the nearest neighbor FM interaction and J_2 is the next nearest neighbor AFM interaction.

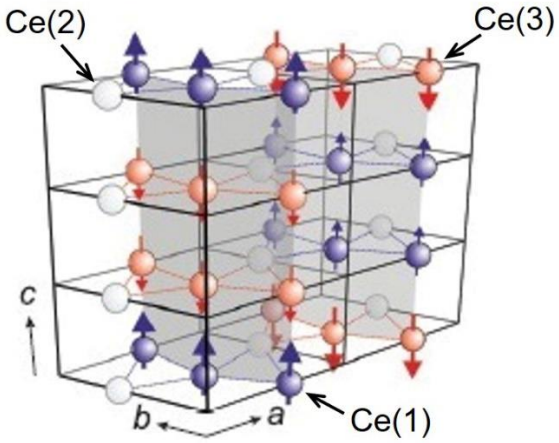

Figure 1.11: The three-dimensional magnetic structure of CePdAl [49]. The AFM ordered planes of Ce (1 and 3) are separated by the paramagnetic plane of Ce(2).

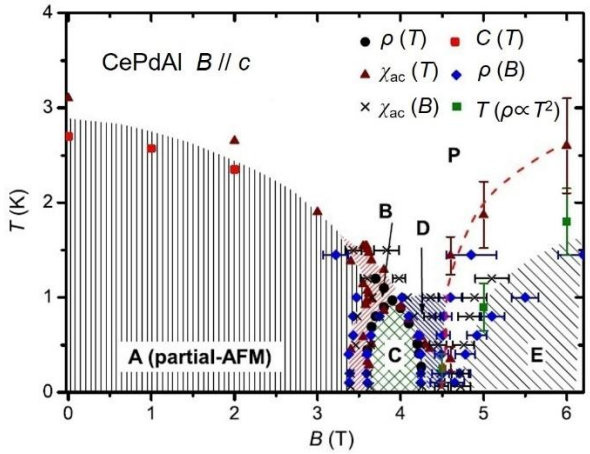

Figure 1.12: B || c vs T phase diagram of CePdAl derived from resistivity, ac susceptibility, and specific heat measurements [64].

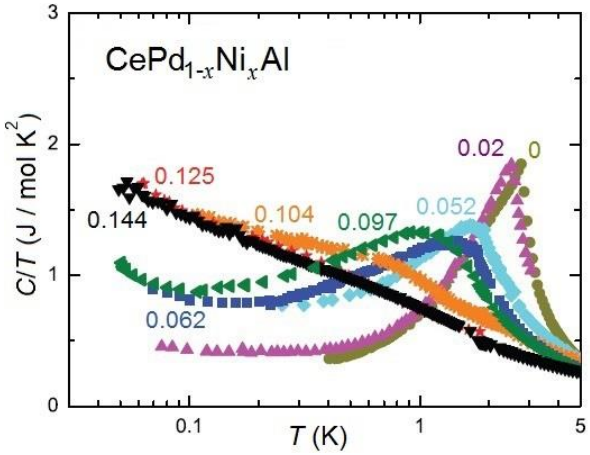

Figure 1.13: Specific heat of $CePd_{1-x}Ni_xAl$ plotted as C/T vs log$T$ [49].

1.2.5 Zero-field quantum criticality in the quasikagome Kondo lattice CeRhSn

In the isostructural compound CeRhSn, layers composed of Ce and Rh1 atoms alternate along the *c* axis with layers composed of Rh2 and Sn atoms as shown in Fig. 1.14(a) [66]. Figure 1.14(b) shows that Ce atoms form a quasikagome lattice in the basal *c* plane. The intraplane Ce-Ce distance of 0.3882 nm is shorter than the interplane Ce-Ce distance of 0.4089 nm. The Ce atom has nearest neighbors of four Rh2 atoms at a distance of 0.3032 nm and second nearest neighbor of one Rh1 atom at 0.3084 nm. In Fig. 1.15, the theoretical calculations of site-projected partial densities of states for CeRhSn show the contribution from Ce itinerant states below Fermi level E_F, which ensure the hybridization with the 4*d* states of Rh and 5*s* and 5*p* states of Sn. The chemical bonding analysis suggests that Ce-Rh are strongly bonding from bottom of valence band up to -2 eV, as shown in Fig. 1.16. All the results mentioned above suggested that the Ce 4*f* state is strongly hybridized with the 4*d* band derived mainly from the Rh atoms, leading to the valence-fluctuating state with a high $T_K \sim 200$ K [67, 68, 69, 70].

As shown in Fig. 1.17, C/T turns up below 7 K in proportion to $-\ln T$ and is saturated to a large value of 200 mJ/K^{2}mol at 0.5 K. In Figs. 1.18 and 1.19, $\chi_c(T)$ and $\rho(T)$ exhibit NFL behaviors down to 0.5 K, respectively. The $\chi(T)$ shows a power-law behavior T^{-n} (n =1.1) for $B \parallel c$ and $\rho(T)$ decreases with T^n ($n \leq 1.5$). These NFL behaviors are thought to be the manifestation of the frustration of Ce moments which hinders the long-range order [68]. In fact, no magnetic order down to 0.05 K was observed by μSR experiments [71].

Recently, a zero-field quantum criticality has been indicated by the measurements of specific heat C and magnetic Grüneisen ratio $\Gamma_H = -(\partial M/\partial T)/C$ down to 0.06 K as shown in Figs. 1.20 and 1.21, respectively [72]. In zero fields, C/T diverges on cooling below 0.7 K. In weak fields, Γ_H/H shows divergence behavior below 0.7 K. In Fig. 1.22, the thermal expansion coefficient α divided by temperature, α/T, displaying the critical behavior only along the *a* axis is in support of the fact that the quantum criticality is driven by the geometrical frustration in the quasikagome lattice.

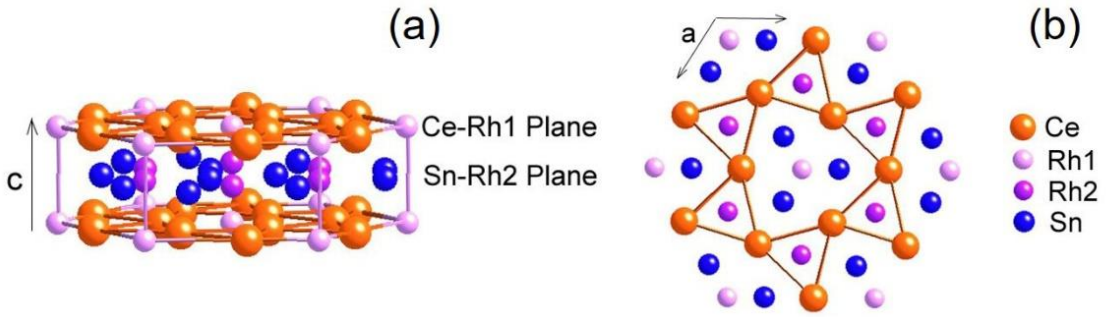

Figure 1.14: (a) Crystal structure of CeRhSn with alternately stacked layers of Ce-Rh1 and Rh2-Sn. (b) Basal *c* plane with quasikagome lattice formed by Ce atoms [66].

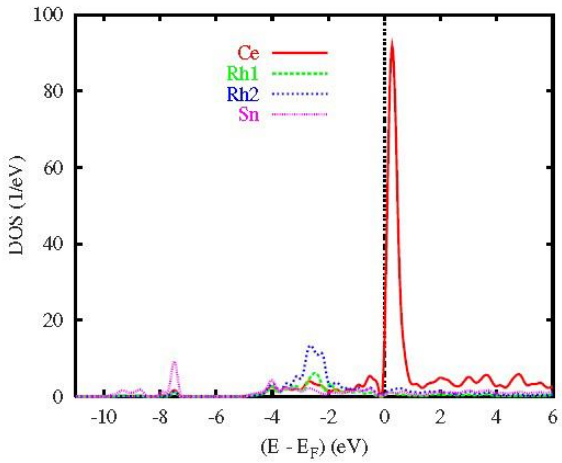

Figure 1.15: Nonmagnetic site-projected densities of states of CeRhSn. The Fermi level E_F is set as zero energy [69].

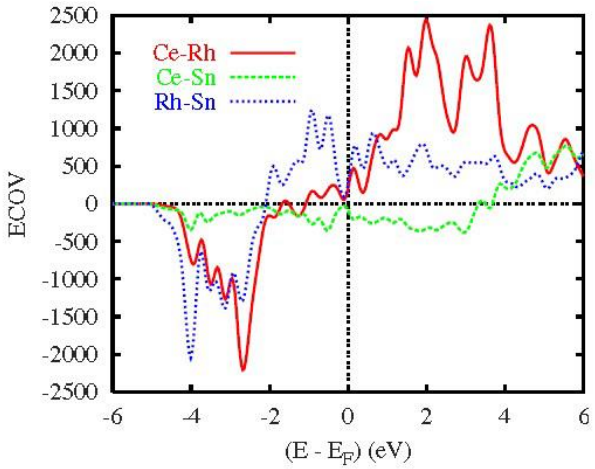

Figure 1.16: The covalent bond energies ECOV for different pairs of orbitals within CeRhSn. The contributions of Rh1 and Rh2 are combined to keep the representation simple [69].

.

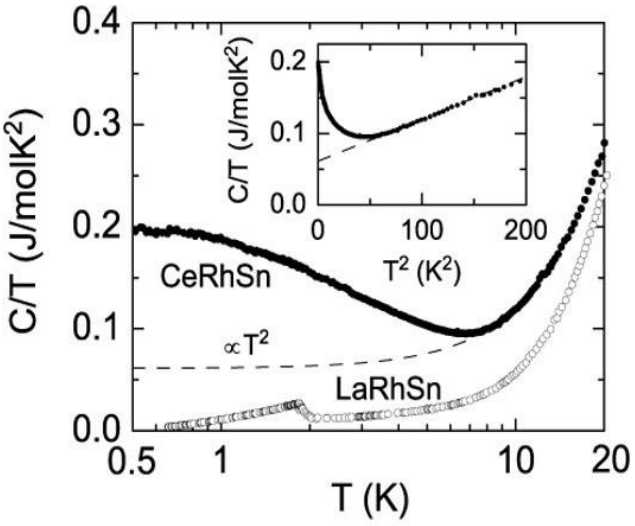

Figure 1.17: Specific heat of single crystal CeRhSn down to 0.5 K plotted as C/T vs log$T$. The inset shows the plot of C/T vs T^2 [68].

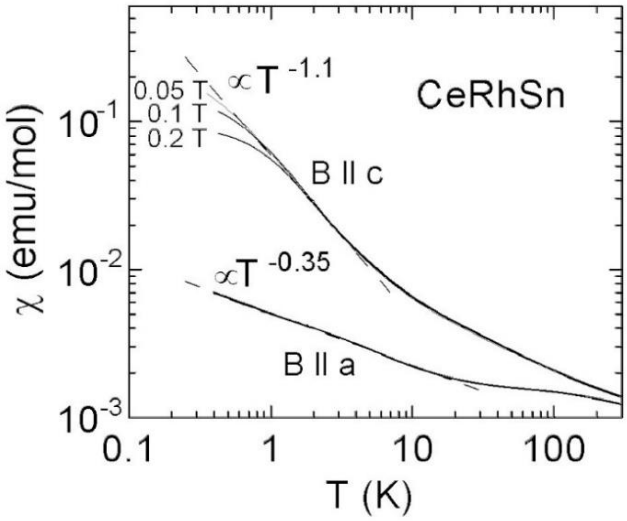

Figure 1.18: Double logarithmic plot of the magnetic susceptibility $\chi(T)$ vs T for the single crystal CeRhSn in $B \parallel c$ and $B \parallel a$ [68].

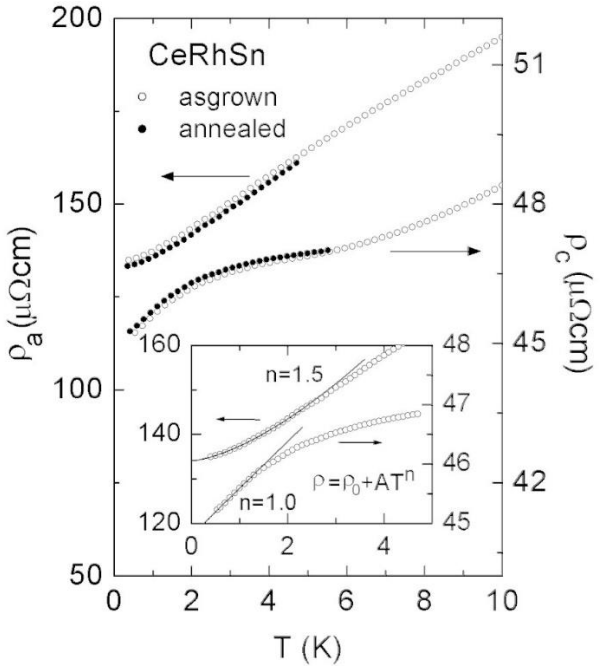

Figure 1.19: Temperature dependence of electrical resistivity $\rho(T)$ for single crystal CeRhSn with current I applied along the a and c axes, respectively [68].

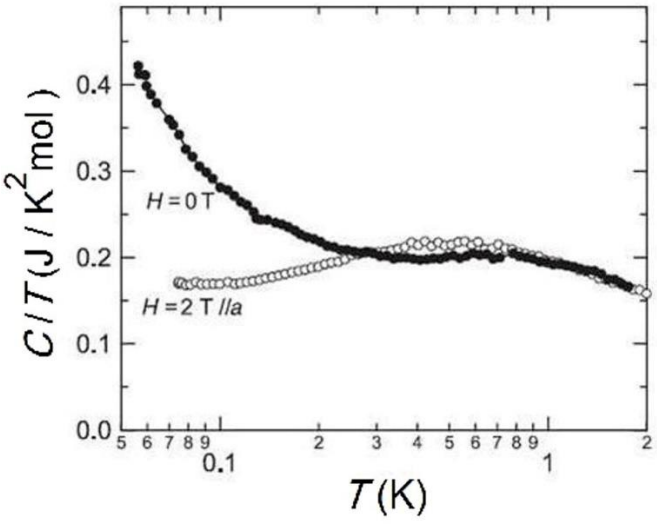

Figure 1.20: Specific heat of single crystal CeRhSn plotted as C/T vs log$T$ down to 0.06 K in magnetic field B || a [72].

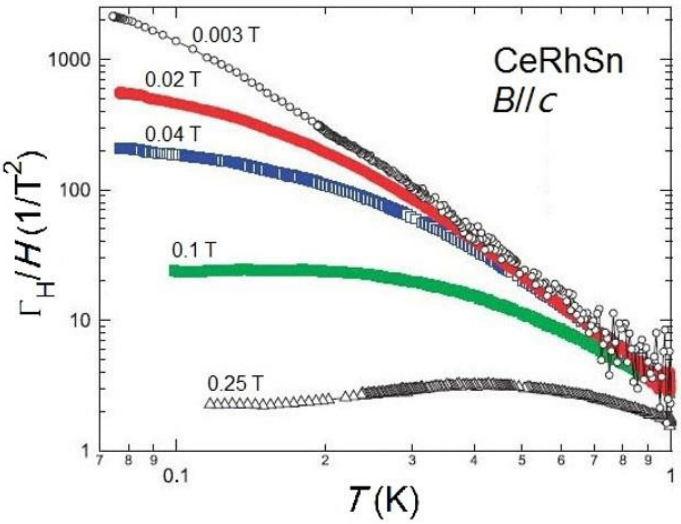

Figure 1.21: Temperature dependence of magnetic Grüneisen ratio for CeRhSn plotted as Γ_H/H vs log$T$ at various magnetic fields applied along the c axis [72].

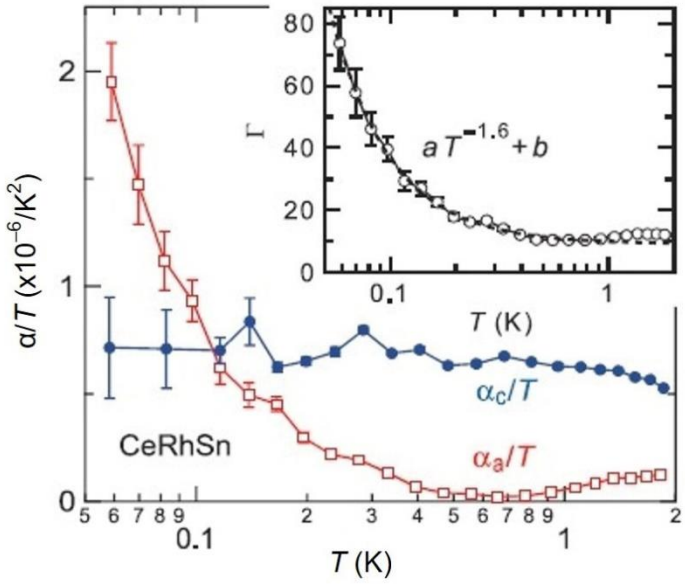

Figure 1.22: Uniaxial thermal expansion coefficient α/T for CeRhSn along the a and c directions, respectively [72]. The inset shows the Grüneisen parameter $\Gamma = BV_m(2\alpha_a+\alpha_c)/C$, where B is bulk modulus of isostructural UCoAl [73], V_m is the molar volume, and C is specific heat.

1.3 Low-dimensional Ce-based heavy fermion compounds

Low-dimensional Ce-based heavy fermion systems have attracted a lot of interests for extoic magnetic and superconducting properties. For example, a quasi-2D heavy fermion compound $CeRhIn_5$ with alternating layers of $CeIn_3$ and $RhIn_2$ along the tetragonal *c*-axis shows a pressure-induced transition from an AFM state to an unconventional superconducting state [74].

Furthermore, there are antiferromagnets with one-dimensional Ce chains. For example, $CePt_5Ge_3$ with the YNi_5Si_3-type orthorhombic structure has a shorter Ce-Ce distance in the chain along the *b* axis that is 70% of the interchain Ce-Ce distance [75]. As shown in Fig. 1.23, above the 3D long-range order at T_N = 1.1 K, a pronounced tail appears in the magnetic specific heat $C_m(T)$ from T_N up to 5 K. The tail of $C_m(T)$ was attributed to the AFM short-range correlations because $C_m(T)$ was well fit by the model with S =1/2 AF uniform Heisenberg chain with the exchange interaction J/k_B = 3.35 K [76, 77]. The magnetic entropy S_m reaches Rln2 only at 5 K. Similarly, the $CePd_3X_2$ family with X = In and Al crystallize in the orthorhombic structure (space group *Pnma*). The crystal structure of $CePd_3In_2$ is shown in Fig. 1.24. The Ce-Ce distance in the chain along the *b* axis is shorter than those along other directions [78, 79]. $CePd_3In_2$ undergoes an AFM order at T_N = 2.1 K where the value of S_m is less than 0.8Rln2 as shown in Fig. 1.25 [80]. The $\rho(T)$ is proportional to $-\ln T$ between 20 and 2 K followed with a drop as shown in Fig. 1.26. The reduction of S_m was attributed to the relatively low $T_K \sim 2$ K. The aluminide $CePd_3Al_2$ shows a distortion in the *b* plane where the *b* parameter is smaller than in the In compound [79]. As shown in inset of Fig. 1.27, $\chi(T)$ shows maximum at 1 K. At T > 20 K, $\chi(T)$ obeys a Curie-Weiss law with the effect moment μ_{eff} = 2.55 μ_B and the paramagnetic Curie-Weiss temperature $\theta_p = -22.1$ K. The magnetization $M(B)$ at 0.5 K saturates to 1 μ_B/Ce at 7 T. The $C(T)$ in Fig 1.28 shows an extended tail in prior to the AFM order at T_N = 1 K. The $\rho(T)$ displays an upturn on cooling from 15 down to 1 K. An obvious drop below 1 K is consistent with the peak observed in $C(T)$ as shown in Fig. 1.29. The extended tail in $C(T)$ was regarded as the result of the enhanced Kondo effect with T_K = 5.5 K [79].

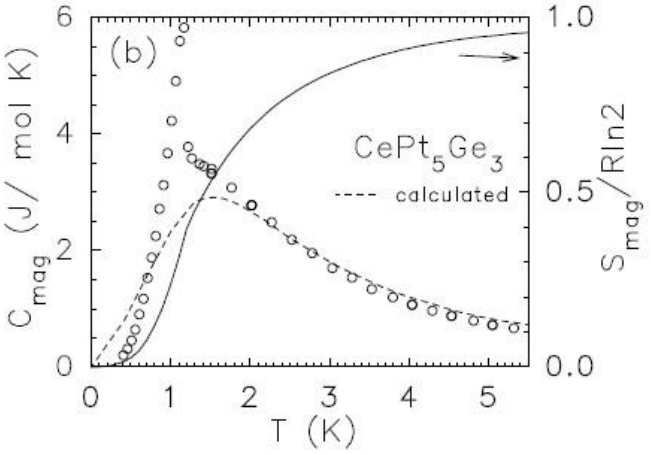

Figure 1.23: Magnetic specific heat C_{mag} and magnetic entropy S_m of $CePd_5Ge_3$ [75].

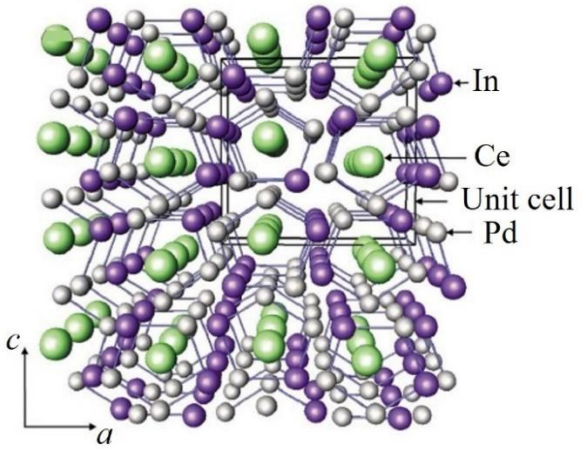

Figure 1.24: Perspective view of the orthorhombic crystal structure of $CePd_3In_2$ along the *b* axis [80].

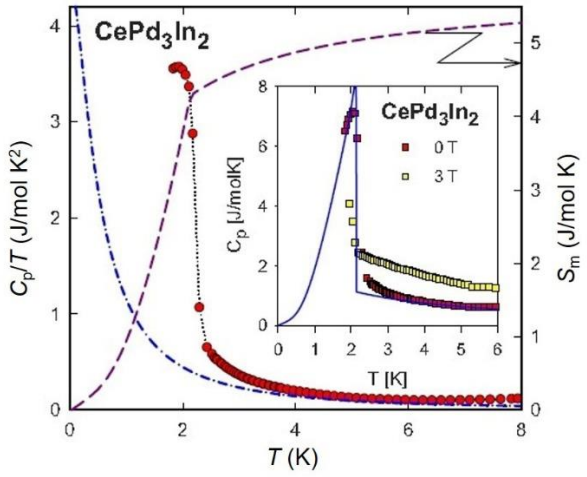

Figure 1.25: Specific heat *C* and magnetic entropy S_m of $CePd_3In_2$ [80].

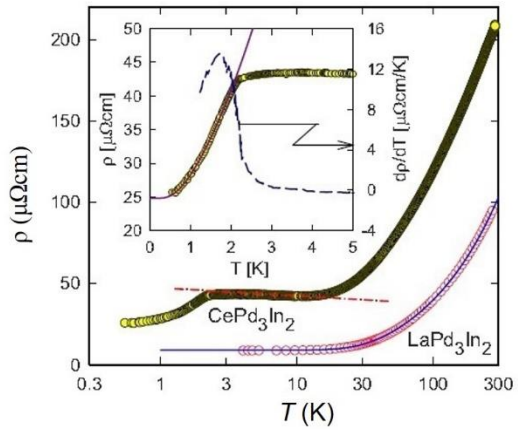

Figure 1.26: Temperature dependence of electrical resistivity of $CePd_3In_2$ and $LaPd_3In_2$ plotted as $\rho(T)$ vs log$T$ [80].

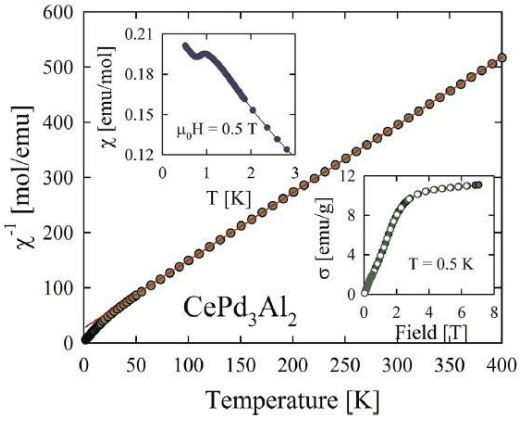

Figure 1.27: Temperature dependence of the inverse of the averaged magnetic susceptibility $\chi(T)$ for $CePd_3Al_2$. Upper inset: $\chi(T)$ for $T < 3$ K. Lower inset: magnetization $M(B)$ at 0.5 K [79].

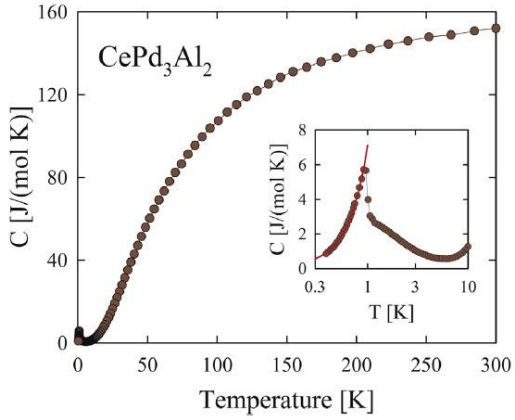

Figure 1.28: Temperature dependence of specific heat C of $CePd_3Al_2$. Inset: low-temperature data plotted as $C(T)$ vs log$T$ [79].

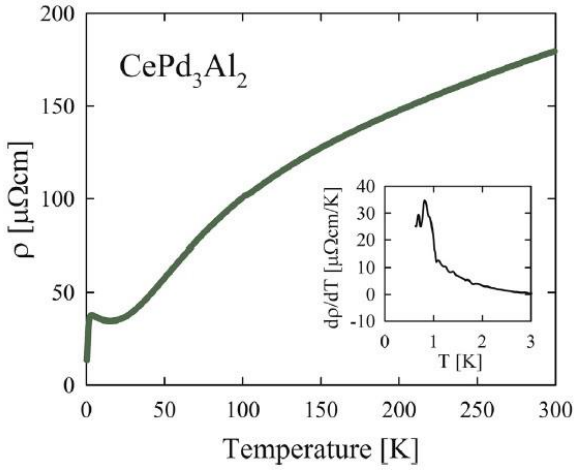

Figure 1.29: Temperature dependence of electrical resistivity $\rho(T)$ of $CePd_3Al_2$. Inset: temperature derivative $d\rho/dT$ at $T < 3$ K [79].

1.4 Purpose of the present study

In order to study the quantum criticality in geometrically frustrated Kondo lattice compounds and low-dimensional compounds, we have chosen cerium-based compounds, CeRhSn and $CePd_3Sn_2$, respectively. Firstly, the issue for the zero-field quantum criticality in CeRhSn is which one is more responsible, geometrial frustration or Kondo effect. In order to do that, we have substituted Pd for Rh in CeRhSn and conducted measurements of magnetic, transport, and specific heat to detect the emerging magnetic order. On one hand, the additional 4*d* electrons are expected to deepen the 4*f* level from the Fermi level, then the hybridization between 4*f* orbitals of Ce and Rh 4*d* orbitals is weakened and Kondo effect is suppressed. On the other hand, the expansion near the doped Pd atoms will break down the local symmetry of the quasikagome lattice, then the geometrical frustration may be released. Secondly, we aim to study the effect of short-range correlations in a new compound $CePd_3Sn_2$ with a chain of Ce atoms along the *b* axis.

Chapter 2

Sample preparation and characterizations

2.1 Sample preparation

2.1.1 $CeRh_{1-x}Pd_xSn$ ($x \leq 0.75$)

Polycrystalline samples with initial compositions of $CeRh_{1-X}Pd_XSn$ ($X = 0, 0.1, 0.2, 0.3, 0.4, 0.5, 0.7, 0.8$) were prepared by arc-melting. The powder of Rh (99.9%) and Pd (99.99%) was pressed into a pellet and melted into a ball of 0.5 g each under a purified argon atmosphere. Appropriate amounts of constituent elements Ce ingot (99.9%), Rh (ball), Pd (ball), and Sn ingot (99.999%) were melted for several times. Figure 2.1 represents the schematic of arc-melting furnace. In order to improve the homogeneity, the ingots were subsequently annealed at 900 °C for 6 days in evacuated quartz ampoules. The total weight loss after preparation was not more than 1%.

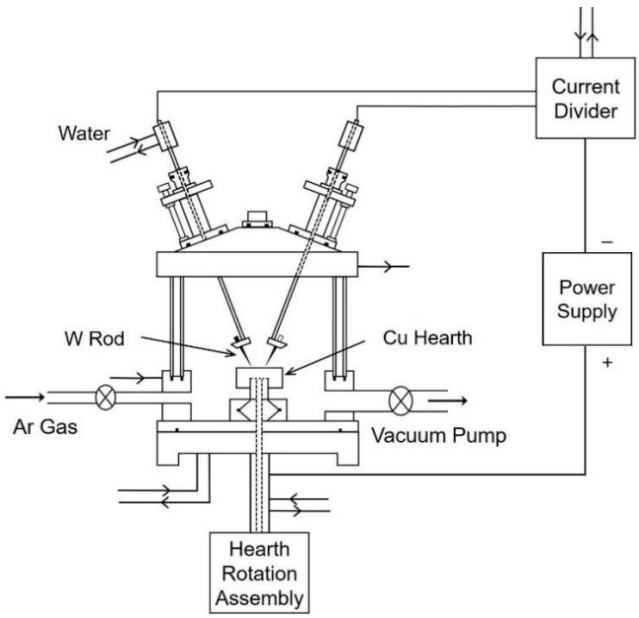

Figure 2.1: Schematic diagram of the arc-melting furnace for the preparation of polycrystalline samples of $CeRh_{1-x}Pd_xSn$.

2.1.2 Single crystal growth of $CeRh_{1-x}Pd_xSn$ (x = 0 and 0.1)

Single crystals of $CeRh_{1-x}Pd_xSn$ (x = 0 and 0.1) were grown by the Czochralski method in an RF induction furnace in an argon gas atmosphere [68]. The schematic diagram and image of the crystal growth are shown in Figs. 2.2 and 2.3. Firstly, the stoichiometric amounts of the constituent elements were melted to be an ingot in a Hukin-type cold crucible. Secondly, the ingot was put in a tungsten crucible and heated to just above the melting point around 1470 ℃. As a seed, a rod of single crystal CeRhSn was fixed on a holder made of molybdenum. The seed was inserted into the liquid by 2-3 mm in depth. Thirdly, the seed was pulled at a speed of 7 mm/h and rotated by 6 rpm. The diameter of the crystal was controlled by regulating the RF power. The image of the as-grown single crystals of $CeRh_{1-x}Pd_xSn$ (x = 0 and 0.1) are represented in Figs. 2.4 and 2.5, respectively.

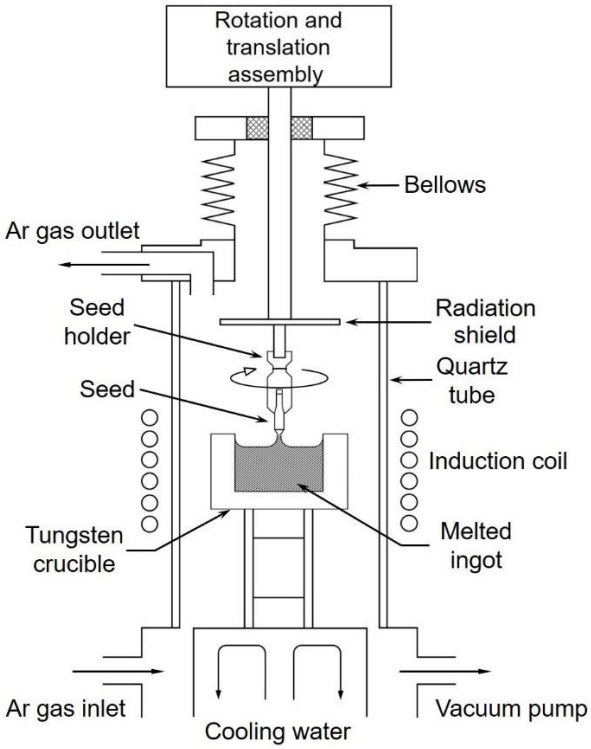

Figure 2.2: Schematic diagram of the radio-frequency induction furnace for the crystal growth of $CeRh_{1-x}Pd_xSn$ (x = 0 and 0.1) by the Czochralski method.

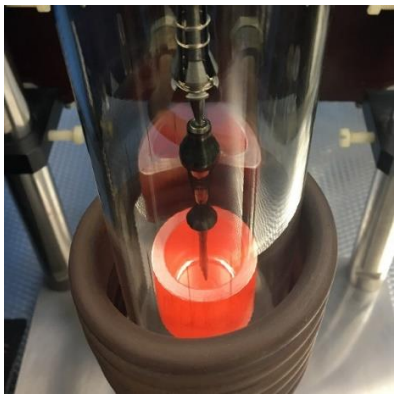

Figure 2.3: Single crystal growth of CeRhSn using the RF furnace by the Czochralski method.

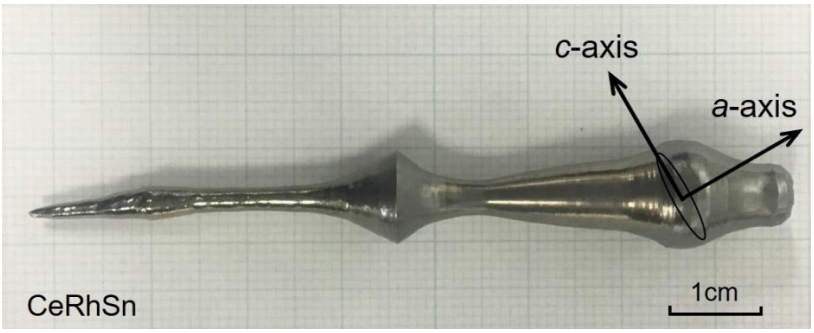

Figure 2.4: Image of the as-grown single crystal CeRhSn.

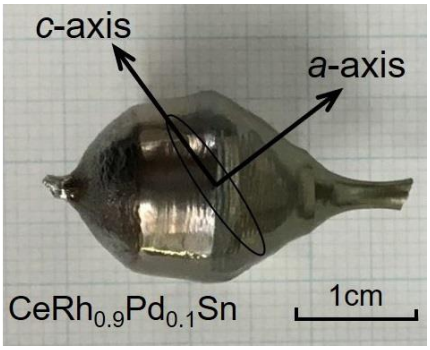

Figure 2.5: Image of the as-grown single crystal $CeRh_{0.9}Pd_{0.1}Sn$.

2.1.3 $CePd_3Sn_2$ and $LaPd_3Sn_2$

Polycrystalline samples of $CePd_3Sn_2$ and its reference compound $LaPd_3Sn_2$ were prepared by arc-melting appropriate amounts of constituent elements Ce (99.9%), La (99.9%), Pd (99.99%), and Sn (99.999%) under a purified argon atmosphere. The ingots were turned over and melted for several times to improve the homogeneity. Subsequently, the ingots were annealed at 900 °C for 6 days in evacuated quartz ampoules. The total weight loss after preparation was less than 1%.

2.2 Characterizations of samples

2.2.1 Metallographic examination and electron-probe microanalysis

The polycrystalline samples $CeRh_{1-X}Pd_XSn$ (X = 0, 0.1, 0.2, 0.3, 0.4, 0.5, 0.7, 0.8) and single crystals $CeRh_{1-x}Pd_xSn$ (x = 0 and 0.1) were characterized by metallographic examination and wavelength-dispersive electron-probe microanalysis (EPMA). As shown in Fig. 2.6, a back scattered electron image of $CeRh_{0.6}Pd_{0.4}Sn$ indicated that the polycrystalline samples are composed of grains of approximately 500 μm in length preferentially oriented along the c axis, which is perpendicular to the bottom surface of the ingot. The value of the Pd composition x determined by EPMA for polycrystalline samples of $CeRh_{1-x}Pd_xSn$ agrees with the nominal composition X in the range of $X \leq 0.5$. However, for $X > 0.5$, it was revealed that the quantity of impurity phase $Ce(Rh_{1-X}Pd_X)_2Sn_2$ increases to approximately 5%. This makes the Pd content x smaller than X, i.e., 0.65 and 0.75 for X = 0.7 and 0.8, respectively. The compositions of both ends of the single crystal rods were examined by EPMA. No impurity phase nor deviation in the stoichiometry was detected within the 1% resolution.

The polycrystalline sample of $CePd_3Sn_2$ is composed of grains larger than 100 μm in length as detected by a polarized light optical microscope image shown in the insert of Fig. 2.10. The values of compositions of constituent elements in $CePd_3Sn_2$ and $LaPd_3Sn_2$ determined by EPMA agree with the nominal compositions.

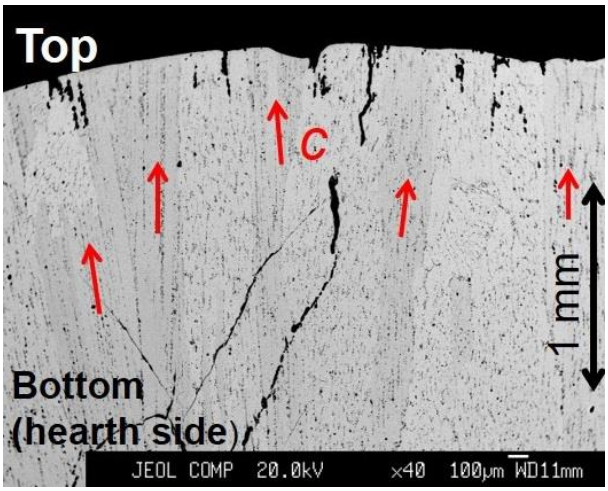

Figure 2.6: Back scattered electron image of the polycrystalline sample $CeRh_{0.6}Pd_{0.4}Sn$. The red arrows indicate the preferentially oriented grains along the c axis.

2.2.2 Powder x-ray diffraction and single crystal x-ray diffraction

Powder x-ray diffraction analysis of the polycrystalline samples $CeRh_{1-x}Pd_xSn$ (x = 0, 0.1, 0.2, 0.3, 0.4, 0.5, 0.65, 0.75) confirmed a single phase of the ZrNiAl-type structure. The x-ray patterns and lattice parameters a and c determined by least-square refinements are plotted in Figs 2.7 and 2.8, respectively. With increasing x up to 0.75, the two parameters both increase by 1.6%. The hexagonal parameter a increases linearly, which is induced by the replacement of Rh atom by Pd atom with a larger atomic radius. Thereby, the local symmetry of quasikagome lattice should be broken. The parameter c deviates from the Vegard' law for x below x = 0.4, which behavior agrees with the previous report [81]. The deviation hints that the 4*f* electron state changes from a valence fluctuating state to a localized state.

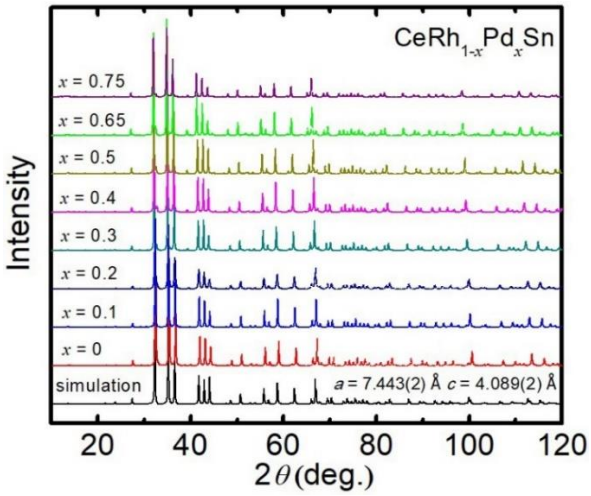

Figure 2.7: Power x-ray diffraction (Cu Kα) patterns of polycrystalline samples $CeRh_{1-x}Pd_xSn$. The bottom one is the simulated pattern.

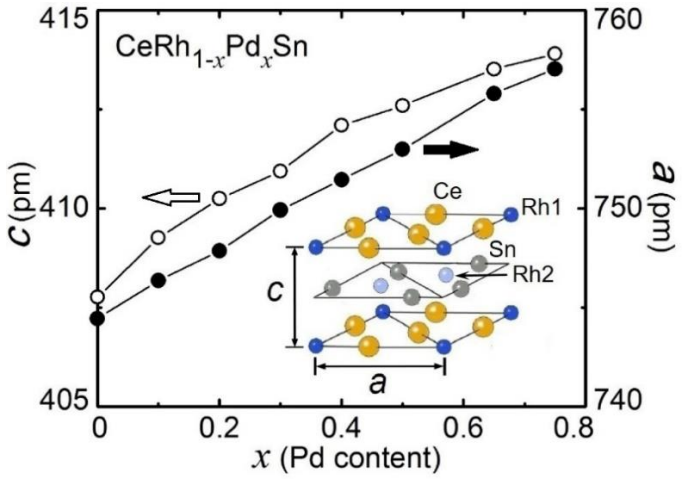

Figure 2.8: Hexagonal lattice parameters a and c of $CeRh_{1-x}Pd_xSn$ as a function of x. The inset shows the unit cell of CeRhSn.

Single crystals of $CePd_3Sn_2$ with a dimeter of approximately 60 μm were isolated via mechanical fragmentation of the annealed polycrystalline sample. X-ray single crystal intensity data were collected at room temperature with a four-circle Nonius Kappa diffractometer with a CCD area detector and graphite monochromated MoKa radiation, λ = 0.071069 nm. The structure was solved by direct methods and refined with the SHELXS-97 and SHELXL-97 programs [82]. The results are summarized in Tables 2.1 and 2.2. The analysis revealed that $CePd_3Sn_2$ crystallizes in an orthorhombic structure with space group *Pnma* (space group No.62), which is isotypic to the $CePd_3In_2$-type [78]. All atomic positions in 4c sites, one site for Ce, three sites for Pd, and two sites for Sn, are fully occupied. Figure 2.9 shows a perspective view of the structure of $CePd_3Sn_2$ along the *b* axis. In the *b* plane, the Pd and Sn atoms form a network of interconnected pentagons with the Ce atoms sitting in the center. The Ce atoms form a chain along the *b* axis with Ce-Ce distance equal to *b* = 0.47663(1) nm, which is shorter compared with the nearest interchain Ce-Ce distance 0.539976(5) nm. The equivalent displacement parameter for the Ce atom is comparable with those of other atoms, indicating the absence of the so called rattling features. A Rietveld refinement of the XRD pattern based on the structural data confirms the structure solution as shown in Fig. 2.10. A polarized light optical microscope image of the polycrystalline sample is represented in the inset, showing grains larger than 100 μm.

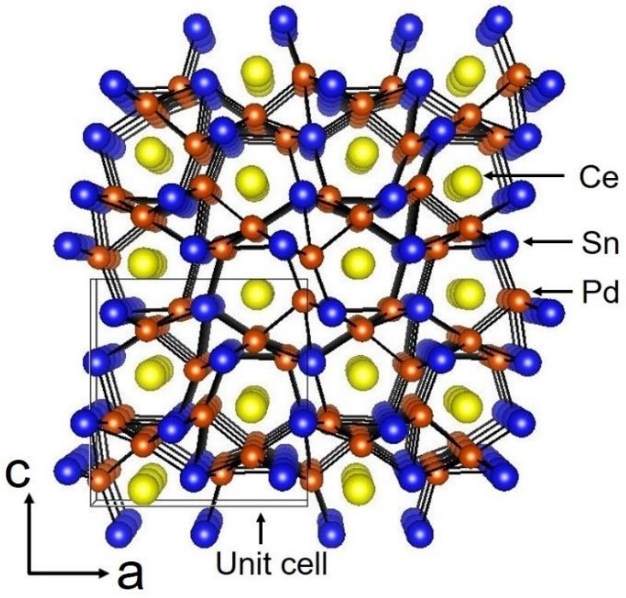

Figure 2.9: Perspective view of the crystal structure of $CePd_3Sn_2$ along the orthorhombic *b* axis. The Ce atoms form a chain along the *b* axis.

Table 2.1: Crystallographic data and structural refinement parameters of $CePd_3Sn_2$.

Composition from EPMA	$CePd_3Sn_2$
Single crystal dimensions (μm)	55 × 60 ×70
Temperature (K)	298
Radiation, λ (nm)	Mo Kα, 0.071069
Crystal system, Person symbol	Orthorhombic, 62
Space group	*Pnma*
Number of formula units in unit cell: Z	4
Unit cell dimensions (nm)	
a	0.97289(1)
b	0.47663(1)
c	1.01692(1)
Cell volume (nm^3)	0.471555
Calculated density (g/cm^3)	9.814
Absorption coefficient μ_{abs} (mm^{-1})	30.88
Max in *hkl*	16, 7, 16
Reflections in refinement	$1202 \geq 4\sigma(F_o)$ of 1221
Total no. reflections	19371
Refined parameters no.	38
$R_F = \Sigma\|F_0^2-F_c^2\|/\Sigma F_0^2$	0.0262
Unique reflections, R_{Int}	0.0349
wR2	0.0830
Goodness-of-fit on F^2	1.256
Extinction (Zachariasen)	0.0034(2)

Table 2.2: Atomic coordinates and equivalent displacement parameters for $CePd_3Sn_2$.

Atom	Wyckoff Site	*x*/*a*	*y*/*b*	*z*/*c*	U_{eq} (nm^2)
Ce	4c	0.23860(5)	1/4	0.06824(4)	0.000071(1)
Pd1	4c	0.48160(7)	1/4	0.59692(7)	0.000102(1)
Pd2	4c	0.25341(6)	1/4	0.77472(6)	0.000084(1)
Pd3	4c	0.10029(7)	1/4	0.36157(8)	0.000134(2)
Sn1	4c	0.02143(6)	1/4	0.63017(5)	0.000074(1)
Sn2	4c	0.38723(6)	1/4	0.35159(5)	0.000073(1)

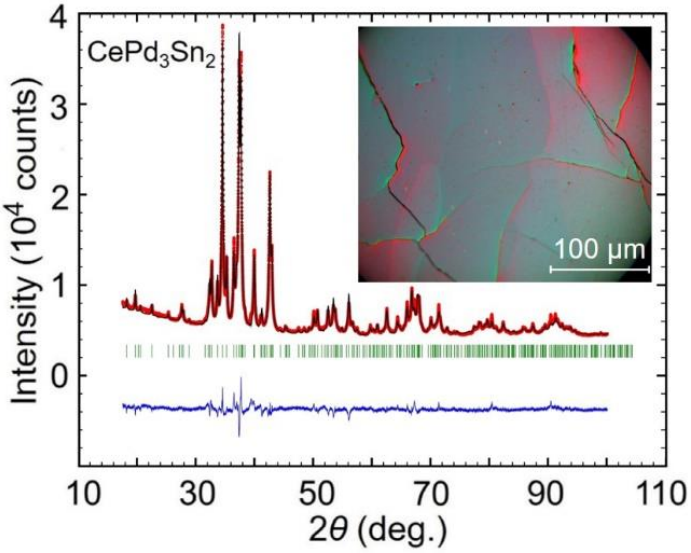

Figure 2.10: Rietveld refinement of powder x-ray diffraction pattern of $CePd_3Sn_2$. Experimental pattern is in red, calculated pattern in black, and difference curve in blue. The green vertical ticks represent Bragg reflections expected for $CePd_3Sn_2$. The inset shows the optical microscope image with polarized light.

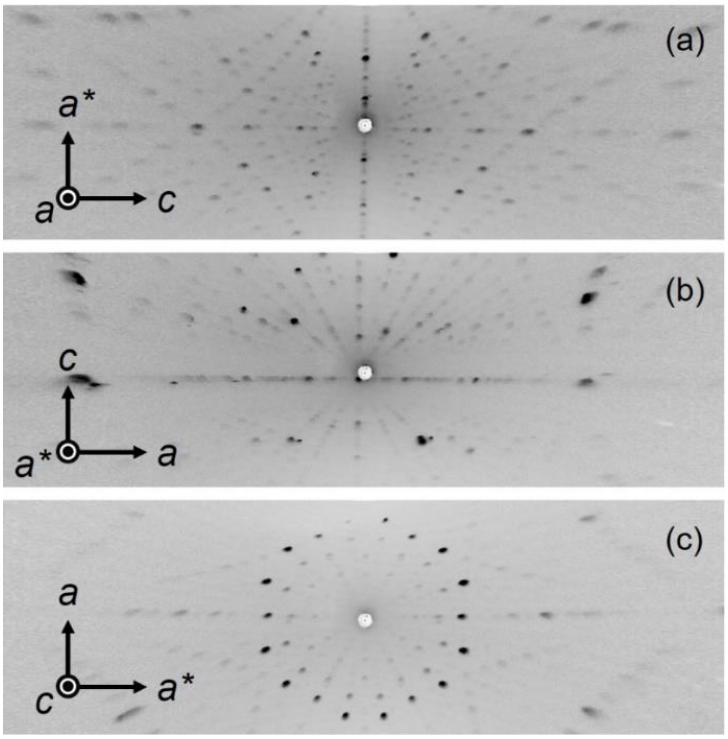

Figure 2.11: x-ray Laue pictures (a), (b), and (c) of single crystal CeRhSn oriented in *a* [110], *a** [100], and c [001] axes, respectively, of the hexagonal ZrNiAl-type structure.

2.2.3 Orienting crystal direction

As shown in Fig. 2.11, the single crystals $CeRh_{1-x}Pd_xSn$ (x = 0 and 0.1) were oriented along the a, a*, and c axes by taking x-ray Laue pictures. The Laue pictures were taken on spots of the polished plane to confirm the alignment of the crystal axis. We confirmed the x-ray Laue patterns parallel to threes axes to correspond with the simulated patterns [68], respectively, shown in Fig. 2.12. Then, the crystals were cut by a spark erosion machine for the measurements of magnetic, transport, and thermal properties.

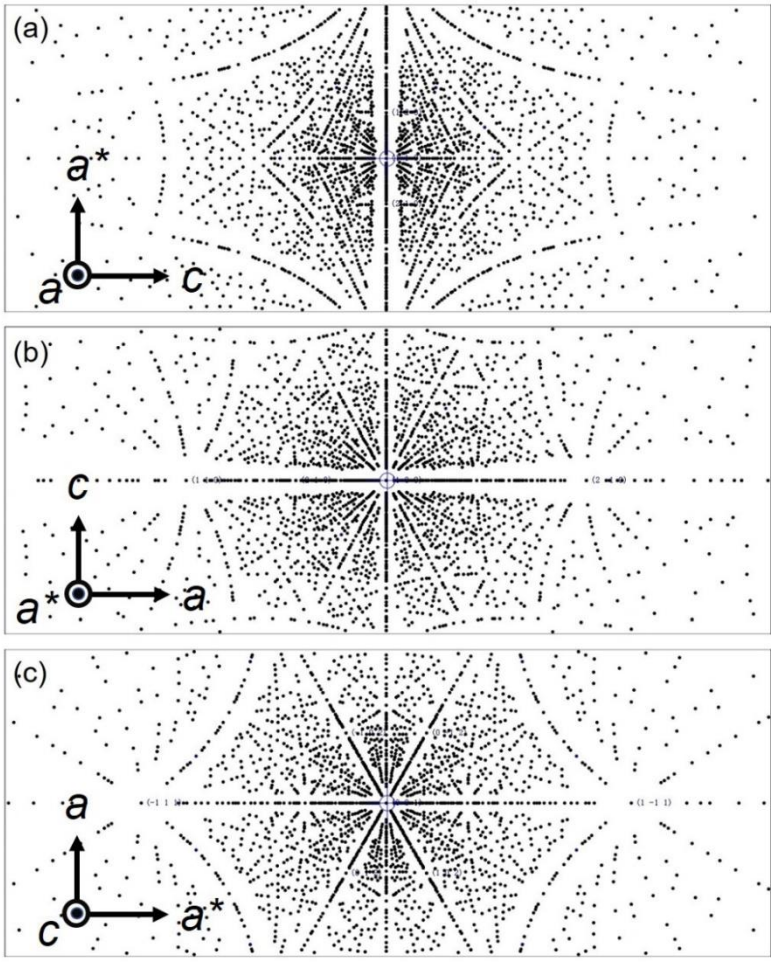

Figure 2.12: Simulated x-ray Laue patterns (a), (b), and (c) for single crystal CeRhSn oriented in a [110], a* [100], and c [001] axes, respectively, of the hexagonal ZrNiAl-type structure.

Chapter 3

Experimental details

3.1 Measurements of magnetic, transport, and thermal properties

3.1.1 Magnetic susceptibility

Because CeRhSn exhibits uniaxial magnetic anisotropy, $\chi(B \parallel c) > \chi(B \perp c)$ [68], dc susceptibility $\chi_{dc}(T)$ of polycrystalline samples $CeRh_{1-x}Pd_xSn$ were measured in two configurations with external fields B = 1 T parallel and perpendicular to the preferred oriented direction in a Quantum Design MPMS from 1.8 to 300 K. The averaged value, $\{\chi(B \parallel) + 2\chi(B \perp)\}/3$, was taken as χ_{dc} to minimize the effect of anisotropy. The magnetization $M(B)$ of polycrystalline samples $CeRh_{1-x}Pd_xSn$ were measured at T = 1.8 K with increasing B up to 5 T. The measurements of $\chi_{dc}(T)$ and $M(B)$ were performed with a MPMS from 300 to 1.8 K and a homemade Faraday force magnetometer in a ^{3}He cryostat down to 0.3 K in fields up to 9.5 T with a gradient of dB/dz = 10 T/m [83]. The temperature- and magnetic-field dependences of χ_{ac} were measured under B_{ac} = 372 μT at the frequency of 67.2 Hz in an OXFORD ^{3}He-^{4}He dilution refrigerator.

The Faraday force magnetometer is shown in Figs. 3.1 and 3.2. One variable plate of a parallel-plate capacitor was suspended by phosphor bronze wires on a load-sensing device. The sample is glued on the variable plate, which thermally connects with a sample thermometer by Cu foil. When a magnetic field gradient G = dB/dz is vertically induced in the sample space, the variable plate descends due to a downward force $F = MG$ on the sample to balance with the restoring force of spring wires $F = k\Delta L$, where k is the stiffness coefficient of phosphor bronze wires. The displacement ΔL is detected by the change of capacitance $C = \varepsilon_0 S/L$ with the relationship $\Delta L = \varepsilon_0 S(1/C_0 - 1/C_z)$, where ε_0 is vacuum permittivity and S is the area of plate.

The magnetization M is obtained by the formula $M = \varepsilon_0 S(1/C_0 - 1/C_z)k/G$. In order to get the absolute value of $M(B)$, the $M(B)$ data measured by MPMS at 1.8 K is used to compare and calculate the k. In addition, the capacitance C is measured by a capacitance bridge with a high solution, 5×10^{-7} pF, which is sensitive for the infinitesimal displacement of the sample.

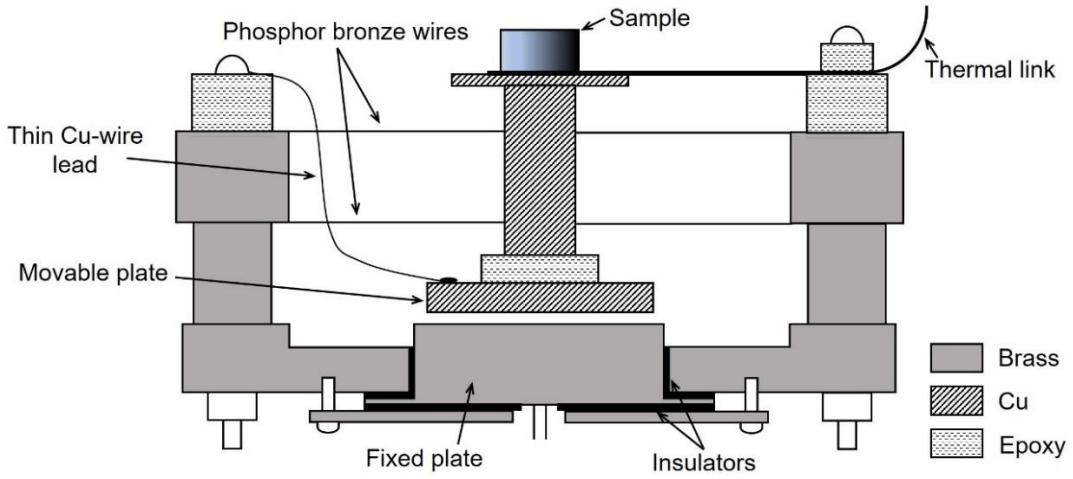

Figure 3.1: Cross profile of the load-sensing device for the capacitive magnetometer. The movable is suspended by four wires of phosphor bronze.

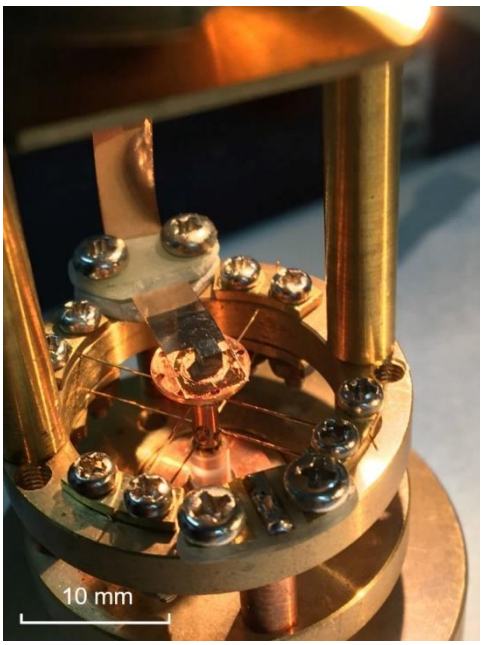

Figure 3.2: Magnetization measurement setup for the single crystal $CeRh_{0.9}Pd_{0.1}Sn$ on the capacitive magnetometer adapted to the ^3He pot of the Heliox, Oxford.

3.1.2 Electrical resistivity

Depending on the temperature and field ranges, the electrical resistivity $\rho(T)$ was measured by a four-probe ac method with different refrigerators. From 2.6 to 300 K, we used a Gifford-McMahon-type refrigerator, whereas from 0.04 to 6 K we used a laboratory-built system installed in the adiabatic demagnetization refrigerator, mF-ADR50. The magnetoresistance $\rho(B, T)$ was measured in both longitudinal and transverse configurations. Up to 14 T down to 2 K we used a Quantum Design PPMS, while up to 17.5 T at 0.08 K we used a ^{3}He-^{4}He dilution refrigerator at Tsukuba Magnet Laboratory, NIMS.

3.1.3 Specific heat

The specific heat $C(T)$ was measured by a thermal relaxation method. The ^{3}He option in a Quantum Design PPMS was used from 0.4 to 300 K while adiabatic demagnetization refrigerator, mF-ADR50 was used from 0.08 to 0.7 K.

The schematic diagram of a calorimeter puck matched to ^{3}He insert is shown in Fig. 3.3 and 3.4 [84]. A sample of about 10 mg is mounted on the platform with Apiezon N-grease. Instead of eight wires used in standard heat capacity puck. this platform is suspended by four wires serve as the electrical leads for a heater and a thermometer which are fixed on the reverse side of platform. These wires only have half of the cross-sectional area of the wires used in standard puck and can provide better thermalization of the sample and platform. A protective cap is design to twist onto the puck for preventing the sample to slip off from the platform.

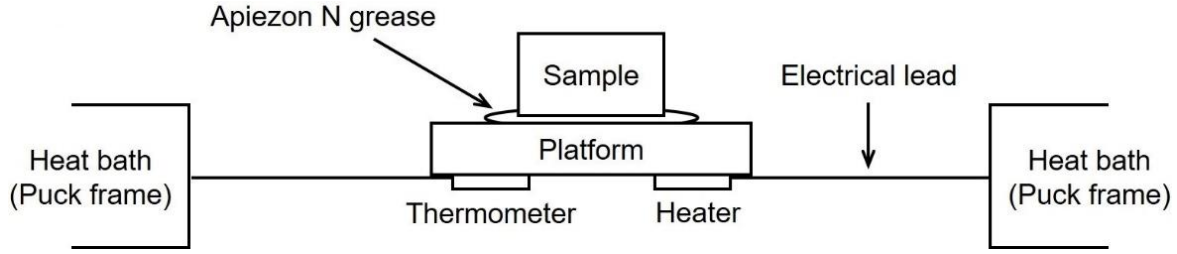

Figure 3.3: Thermal connections from the heat bath to the sample and sample platform in the calorimeter puck matched to ^{3}He insert of PPMS.

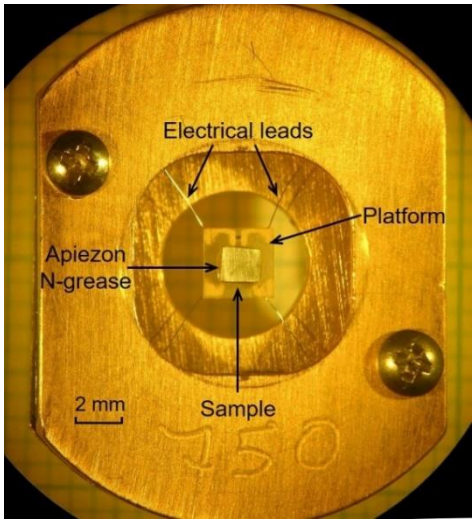

Figure 3.4: Specific heat measurement setup for the polycrystalline sample $CeRh_{0.7}Pd_{0.3}Sn$ on the platform of the calorimeter puck (#750) matched to ^{3}He insert of PPMS.

The principle of relaxation process of heat for the specific heat measurement is shown in Fig. 3.5. The heat capacity option controls the heat added to and removed from the sample while monitoring the change of temperature T. The K_1 and K_2 are thermal conductances between the sample platform and the puck frame due to supporting wires and between the sample platform and the sample by the grease, respectively. During heating portion, a constant power P_0 is applied on the platform. If the K_2 is large enough, sample and sample platform are at same temperature. A simple model is used to analyze the heat capacity of sample platform and sample. The thermal balance equations for the heating portion and saturation one are, respectively, given as below

$$P_0 = \left(C_\mathrm{s} + C_\mathrm{p}\right)\frac{\mathrm{d}T}{\mathrm{d}t} + K_1(T - T_0), \tag{3.1}$$

$$P_0 = K_1(T - T_0) = K_1 \Delta T, \tag{3.2}$$

where C_s and C_p are the heat capacities of sample and platform, respectively, and T_0 is the puck frame temperature. After the temperature increases to T_1 followed the cooling portion, the thermal balance equation is described as

$$\left(C_\mathrm{s} + C_\mathrm{p}\right)\frac{\mathrm{d}T}{\mathrm{d}t} = K_1(T - T_1), \tag{3.3}$$

then get the time dependence of temperature as

$$T(t) = T_0 + \Delta T e^{-\frac{t}{\tau}}, \tag{3.4}$$

$$\tau = (C_s + C_p)/\, K_1. \tag{3.5}$$

We can calculate the thermal conductance K_1 from the Eq. 3.2 from a known P_0 and measured ΔT. Relaxation time τ is obtained by fitting the relaxation curve in terms of Eq. 3.4. After subtracting the heat capacity of sample platform with grease, we evaluate the specific heat of the sample.

If the thermal contact between the sample platform and the sample is poor, there is a temperature difference between the two, T_p and T_s. The two-tau model is described as

$$P(t) = C_p \frac{dT_P}{dt} + K_1(T_p - T_0) + K_2(T_p - T_s), \tag{3.6}$$

$$C_s \frac{dT_s}{dt} = K_2(T_p - T_s), \tag{3.7}$$

where P(t) is P_0 during heating portion and equals zero during cooling portion. Then, we get the solution of time dependence of platform temperature

$$T_P(t) = T_0 + Ae^{-\frac{t}{\tau_1}} + Be^{-\frac{t}{\tau_2}}, \tag{3.8}$$

After fitting the relaxation curve and subtracting the heat capacity of sample platform, we obtain the heat capacity of sample

$$C_S = K_1\tau_1\left(1 - \frac{K_1\tau_2}{C_P}\right) + K_1\tau_2 - C_P. \tag{3.9}$$

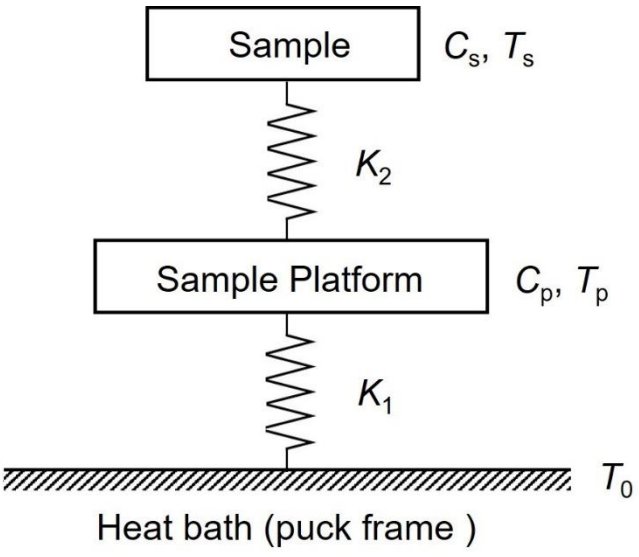

Figure 3.5: Principle of relaxation process of heat for the specific heat measurement.

A home-made calorimeter installed in the mF-ADR50 is shown in Fig. 3.6. The sample platform made of silver is suspended at the center of copper ring by four nylon wires. The sample is thermally contacted with the platform by silver paste. A RuO_2 resistance thermometer and a resistance heater of strain gauge (120 Ω, KFL-02-120-c1-16, KYOWA) are glued on the back of the silver platform by GM vanish. Superconducting wires of Nb_3Sn with ϕ50 μm diameter are served as electrical leads to the thermometer and heater. A copper cap for shielding the radiation is set into the vacuum chamber of the mF-ADR50. A KEITHLEY 6220 current source and a KEITHLEY 2001 multimeter are used to provide the electrical current I and measure the voltage V for the heater, respectively. A LakeShore 370 ac resistance bridge is used to measure the resistance of the thermometer, giving the sample temperature. The schematic of the measurement is shown in Fig. 3.7. The heat capacity of the addenda including the platform and silver paste is measured before the measurements with sample.

Figure 3.8 shows an example of heating and relaxation curve for the polycrystalline sample $CeRh_{0.7}Pd_{0.3}Sn$. We used the simple model to calculate the heat capacity of the sample as describe above. After the sample temperature becomes stable at T_0, the heater is turn on at t_1, then the temperature increases to $T_0+\Delta T$, in which ΔT is set at 2% of T_0. When the temperature is saturated at t_2, the current supply is turned off. Then, the temperature decreases exponentially down to T_0 according to Eq. 3.4.

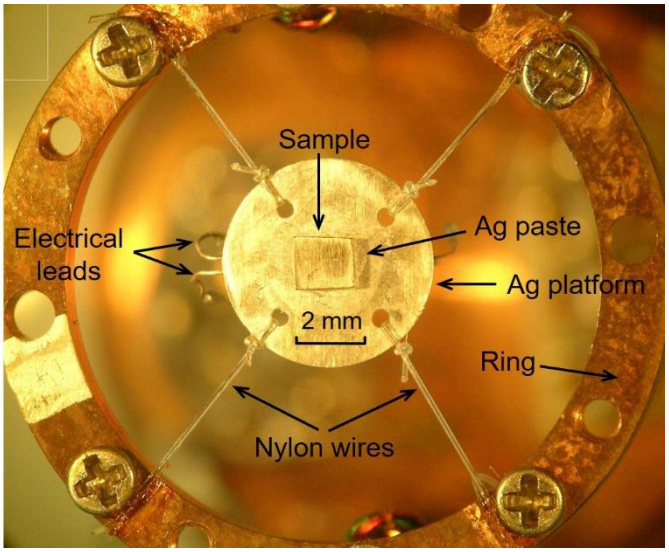

Figure 3.6: Specific heat measurement setup for the polycrystalline sample $CeRh_{0.7}Pd_{0.3}Sn$ with the home-made calorimeter installed in the mF-ADR50.

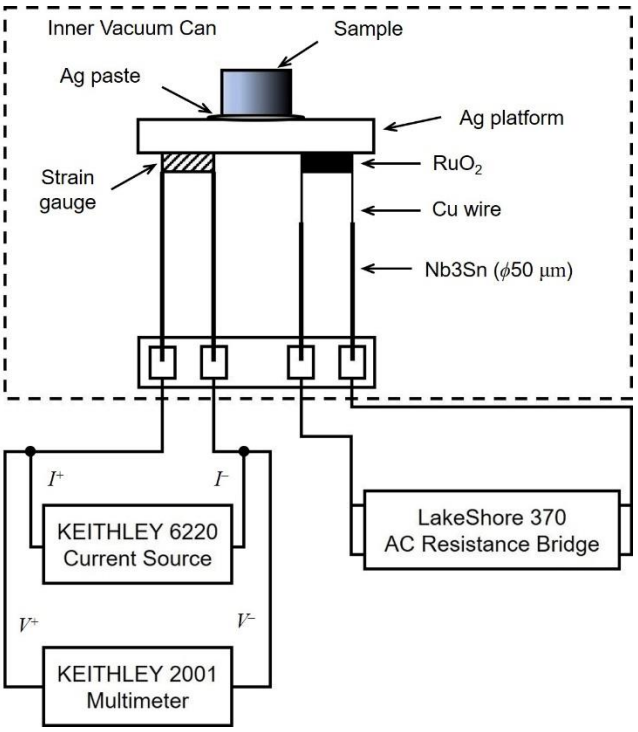

Figure 3.7: Circuit diagram of specific heat measurements with the home-made calorimeter from 0.06 to 0.7 K.

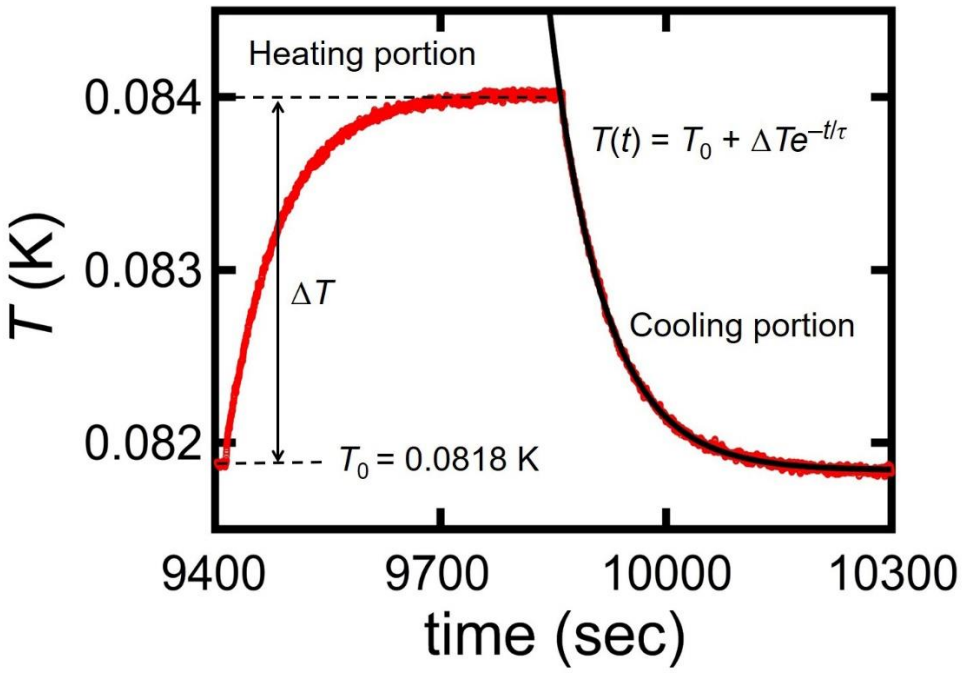

Figure 3.8: Heating and cooling curves of the relaxation method for the polycrystalline sample $CeRh_{0.7}Pd_{0.3}Sn$ with the home-made calorimeter installed in the mF-ADR50.

Chapter 4

Results and discussion

4.1 Magnetic, transport, and thermal properties of $CeRh_{1-x}Pd_xSn$ ($x \leq 0.75$)

The valence of Ce in CeRhSn was evaluated as 3.07 by the Ce3*d* x-ray photoelectron spectroscopy measurements [85]. The possible decrease to 3.0 in the valance of $CeRh_{1-x}Pd_xSn$ at $x = 0.75$ due to the increasing *a* and *c* parameters will be described below in terms of the results of $\chi(T)$ and $M(B)$. The localized magnetic moments in the trivalent state should stabilize a magnetic order at low temperatures.

Magnetic susceptibility

With Pd substitution in $CeRh_{1-x}Pd_xSn$ from 0 to 0.75, a dramatic change in the 4*f* state is expected to manifest itself in the temperature dependence of magnetic susceptibility $\chi(T)$. The inverse of $\chi - \chi_0$ is plotted in Fig. 4.1, where χ is the average $\{\chi(B \parallel) + 2\chi(B \perp)\}/3$ and χ_0 is temperature independent contribution. In the temperature range from 1.8 to 300 K, $\chi(B \parallel)$ and $\chi(B \perp)$ were respectively measured in external fields of 1 T applied parallel and perpendicular to the preferred orientation of the sample along the *c* axis. In Fig. 4.1, the solid lines above 100 K represent the fits with the modified Curie-Weiss formula $(\chi - \chi_0)^{-1} = (T - \theta_p)/C$, where θ_p is the paramagnetic Curie temperature. The fitting parameters of effective magnetic moment μ_{eff}, θ_p, and χ_0, are listed in Table 4.1. For $x = 0$, the large and negative value of $\theta_p = -155$ K and the small value of $\mu_{eff} = 1.42\ \mu_B$ are characteristics of a valence-fluctuating Ce-based compound. With increasing *x* up to 0.5, $|\theta_p|$ gradually decreases to 23 K. This behavior is understood as the suppression of Kondo effect due to the relationship $|\theta_p|/2 \sim T_K$ regardless of frustration effects [86]. For $x \geq 0.65$, μ_{eff} increases nearly to $2.54\mu_B$, which is the expected value for a free Ce^{+3} ion. As shown in the inset of Fig. 4.2, an AFM order in the sample with $x = 0.75$ is indicated by

a maximum at around 3 K in $\chi(B \parallel)$. The magnetic order at round 3 K is not induced by the impurity phase of $Ce(Rh_{1-x}Pd_x)_2Sn_2$ because both end compounds $CeRh_2Sn_2$ and $CePd_2Sn_2$ order antiferromagnetically only below 0.5 K [87].

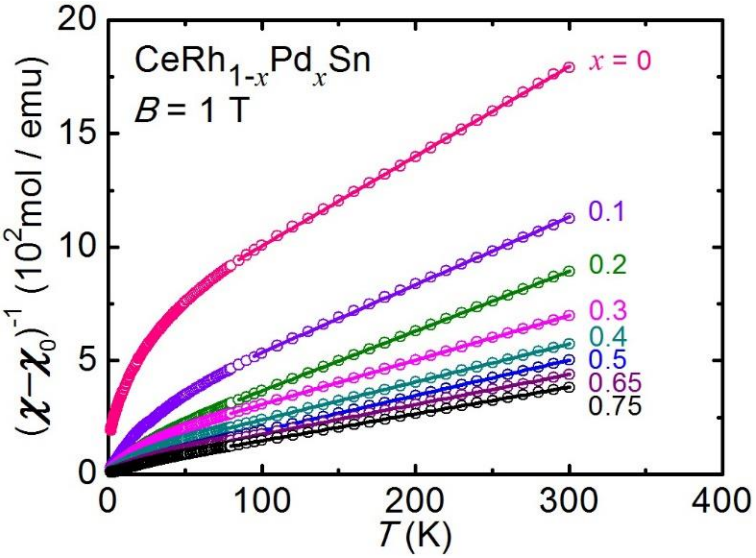

Figure 4.1: Temperature dependence of the inverse of the averaged magnetic susceptibility of $CeRh_{1-x}Pd_xSn$. Solid lines are the fits with the modified Curie-Weiss form $\chi - \chi_0 = C/(T - \theta_p)$ to the data at temperatures above 100 K.

Table 4.1: Parameters obtained by the fits with the modified Curie-Weiss form $\chi = C/(T - \theta_p) + \chi_0$ to the averaged magnetic susceptibility data $\{\chi(B \parallel) + 2\chi(B \perp)\}/3$ at $T > 100$ K. $\chi(B \parallel)$ and $\chi(B \perp)$ were measured, respectively, in external fields of 1 T applied parallel and perpendicular to the samples of $CeRh_{1-x}Pd_xSn$ preferentially oriented along the c axis. μ_{eff}, θ_p, and χ_0 are the effective magnetic moment, paramagnetic Curie temperature, and temperature independnet term, respectively.

Pd content x	Effective moment μ_{eff} (μ_B/Ce)	Paramag. Curie Temp. θ_p (K)	χ_0 (10^{-4}mol/emu)
0	1.42	-155	7.37
0.1	1.64	-80	7.20
0.2	1.74	-40	6.29
0.3	2.02	-57	5.20
0.4	2.19	-43	3.51
0.5	2.27	-23	2.80
0.65	2.47	-34	1.18
0.75	2.60	-25	0

Magnetization

The isothermal magnetization $M(B \parallel)$ of polycrystals was measured at T = 1.8 K under fields up to 5 T. As shown in Fig. 4.2, $M(B \parallel)$ of x = 0 increases almost linearly to a value of 0.05μ_B/Ce at 5 T, which is 67% of the reported value for the single crystal for $B \parallel c$ [68]. It confirms the preferentially oriented of grains along the c axis in the polycrystals. For $x \geq 0.1$, $M(B)$ gradually increases and shows a tendency towards saturation. It is noteworthy that $M(B \parallel)$ for x = 0.75 shows a spin-flop-like upturn at B = 2 T and reaches a saturated value of 1.4 μ_B/Ce at 5 T. This magnitude is close to the saturation moment along the easy c axis in CePdAl with nearly trivalent Ce ions [63]. From the results of magnetic measurements, we consider the reason of an AFM order at x = 0.75. The additional 4*d* electrons may suppress the *c*-*f* hybridization and increase the Ce 4*f* moments. This enhances the RKKY interaction, leading to the AFM order.

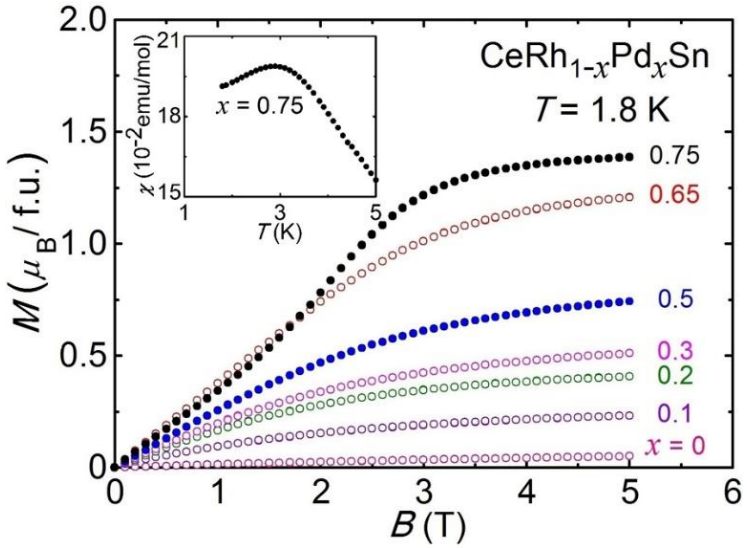

Figure 4.2: Isothermal magnetization curves $M(B \parallel)$ for polycrystalline samples of $CeRh_{1-x}Pd_xSn$ at 1.8 K. The magnetic field B was applied parallel to the preferred orientation of grains. The inset shows the temperature dependence of the magnetic susceptibility for x = 0.75 below 5 K.

Electrical resistivity

Figure 4.3 shows the electrical resistivity normalized to the value at 300 K, $\rho(T)/\rho(300\ \mathrm{K})$, for polycrystalline samples of $CeRh_{1-x}Pd_xSn$ ($x \leq 0.75$). The electrical current I was applied along the bar-shaped samples composed of grains preferentially oriented along the c axis. The values of $\rho(300\ \mathrm{K})$ are in the range between 80 and 140 $\mu\Omega$ cm. For $x = 0$, $\rho(T)$ displays a broad shoulder around 50 K followed by a decrease, which behavior resembles that of the single crystal for $I \parallel c$ shown in Fig. 4.8. For $x = 0.2$ and 0.5, a flat behavior is followed by an upturn at $T < 20$ K, which is likely attributed to incoherent Kondo scattering due to the disorder in the Kondo lattice. With further increasing x to 0.65, a metallic behavior is recovered. For $x = 0.75$, the decrease in $\rho(T)$ at $T < 5$ K hints a sort of magnetic order at lower temperatures.

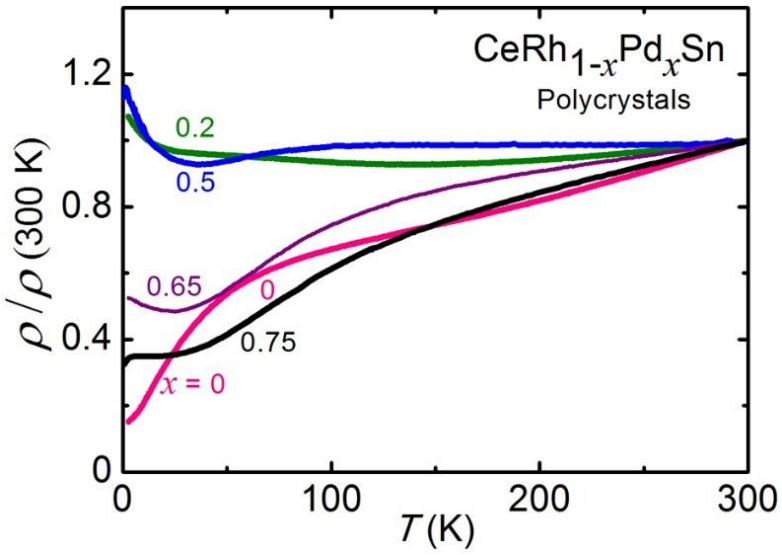

Figure 4.3: Temperature dependence of the electrical resistivity normalized to the value at 300 K for polycrystalline samples of $CeRh_{1-x}Pd_xSn$.

Specific heat and ac susceptibility

Emergence of magnetic order in $CeRh_{1-x}Pd_xSn$ has been revealed by the measurements of specific heat $C(T)$ and $\chi_{ac}(T)$ down to 0.08 K and 0.03 K, respectively. The data of C/T are plotted vs. log$T$ in Fig. 4.4(a), where C/T for $x = 0$ weakly increases on cooling as was reported [72]. On the contrary, C/T for $x = 0.1$ exhibits $-\log T$ dependence, which is followed by a maximum at $T_M = 0.1$ K, suggesting the onset of a magnetic order. The peak temperature T_M increases to 1.0 K with the increase in x to 0.5, where the peak of C/T becomes highest. For $x = 0.75$, two humps are found at 1.2 K and 2.5 K, the latter of which is adopted as T_M because it agrees with the maximum temperature of $\chi_{dc}(B \parallel)$ as seen in the inset of Fig. 4.2. Similarly, $\chi_{ac}(T)$ plotted in Fig. 4.4(b) shows a maximum at T_χ, whose temperature shifts from 0.1 to 0.7 K as x is increased from 0 to 0.4. It is noteworthy that χ_{ac} for $x = 0$ shows a maximum at 0.1 K, whereas C/T does not exhibit a peak down to 0.07 K. The different behaviors might be interpreted as the manifestation of a spin glass state. It is however at variance with the absence of any kind of magnetic order down to 0.05 K as proved by μSR measurements [70]. The nature of the ground state in $CeRh_{1-x}Pd_xSn$ has to be further clarified by microscopic methods with respect to exotic magnetic orderings proposed for kagome Kondo lattice as functions of electron density and Kondo coupling [88, 89, 90].

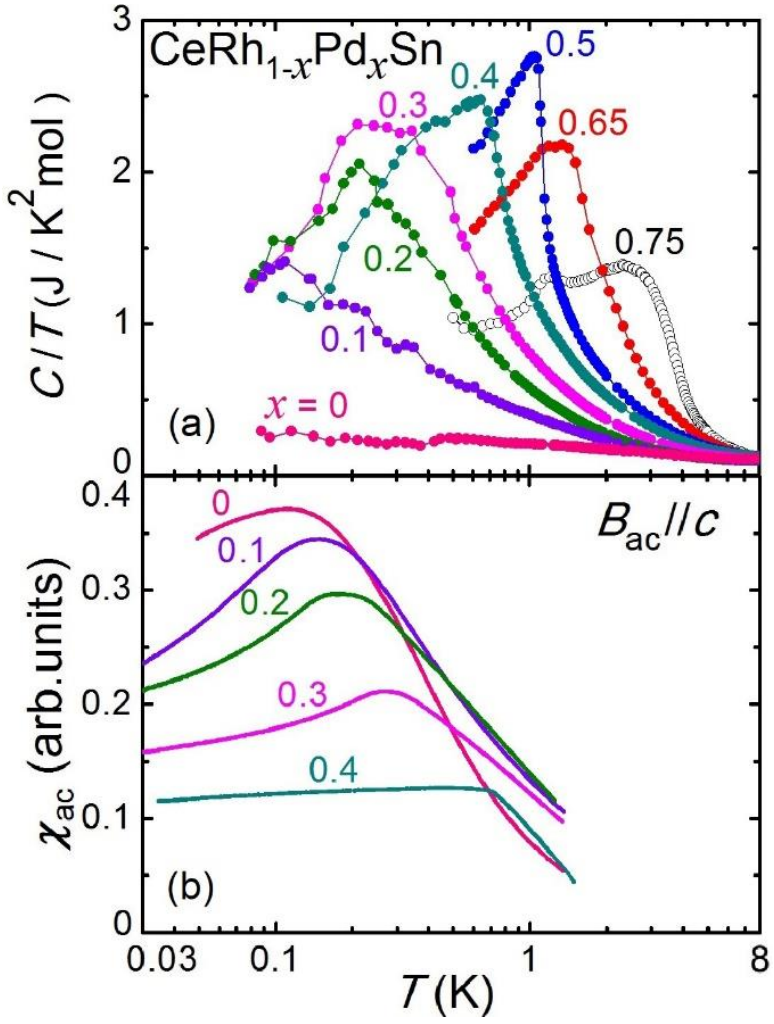

Figure 4.4: (a) Specific heat of polycrystalline samples of $CeRh_{1-x}Pd_xSn$ ($0 \leq x \leq 0.75$) plotted as C/T vs log$T$. (b) ac magnetic susceptibility vs log$T$ for single crystals with $x = 0$ and 0.1 and polycrystals with 0.2, 0.3, and 0.4.

Phase diagram

The temperatures of T_M and T_χ are plotted in Fig. 4.5, constructing a phase diagram of $CeRh_{1-x}Pd_xSn$. For $x = 0.1$, T_χ is higher than T_M but T_χ agrees with T_M in the range $0.2 \leq x \leq 0.4$. The increasing trend of T_M and T_χ suggests that the Pd substitution for Rh suppresses both frustration and Kondo effect, leading to the development of an AFM order. From the bulk measurements presented here, however, it is difficult to separate the two contributions from frustration and Kondo effect. The effect of frustration on the magnetic structure in this system could be elucidated by neutron scattering experiments, as was successfully done for CePdAl [47, 50].

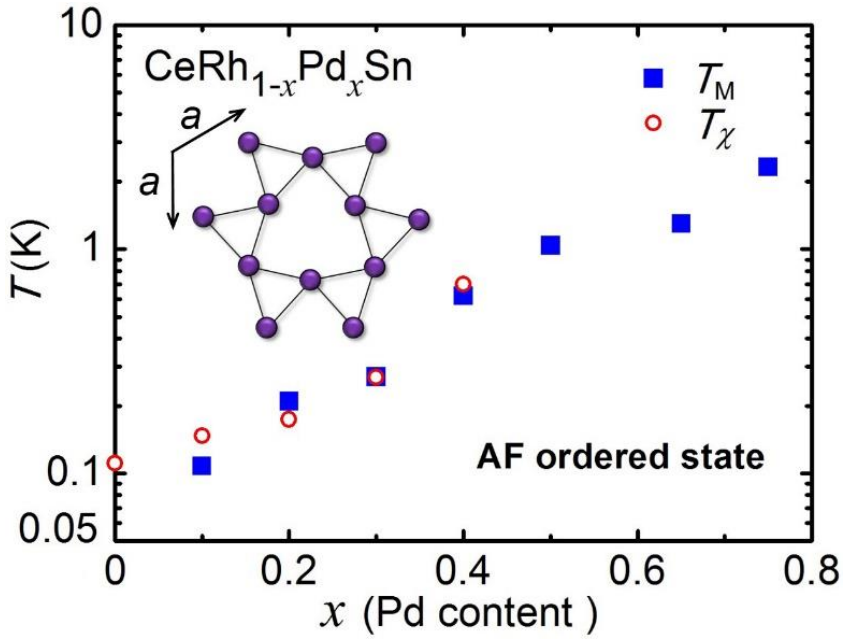

Figure 4.5: Temperatures at the maximum in C/T (■) and $\chi_{ac}(T)$ (○) for $CeRh_{1-x}Pd_xSn$ vs x.

Magnetic entropy

In order to estimate the magnetic entropy $S(T)$, the data of C/T of $CeRh_{1-x}Pd_xSn$ for $x = 0$ and $0.1 \leq x \leq 0.75$ were tentatively extrapolated to $T = 0$ by using the equations $C/T = \gamma + \beta T^2 + CT^2 \ln T$ and $C/T = \gamma + \beta T^2 + \delta T^2 e^{-\Delta/k_B T}$, respectively, which are relevant for a spin-fluctuating system and an antiferromagnet with spin wave excitations with an anisotropic gap [91, 92]. The data of isostructural LaRhSn were used as the phonon contribution to be subtracted from the measured data. We calculated $S(T)$ by integrating the magnetic contribution to C/T and plotted the results in Fig. 4.6. The $S(T)$ curves for $x = 0.65$ and 0.75 are saturated to $R\ln 2$ at around 10 K, confirming the doublet ground state of the Ce ion at the 3*f* site with the local *m*2*m* symmetry under the crystal field. If we neglect the effect of frustration, then T_K can be estimated by using a relation for a Kondo impurity, $S(T_K) = 0.45 = 0.65\ln 2$ [93]. The estimated T_K decreases from 80 K for $x = 0$ to 3 K for $x = 0.5$.

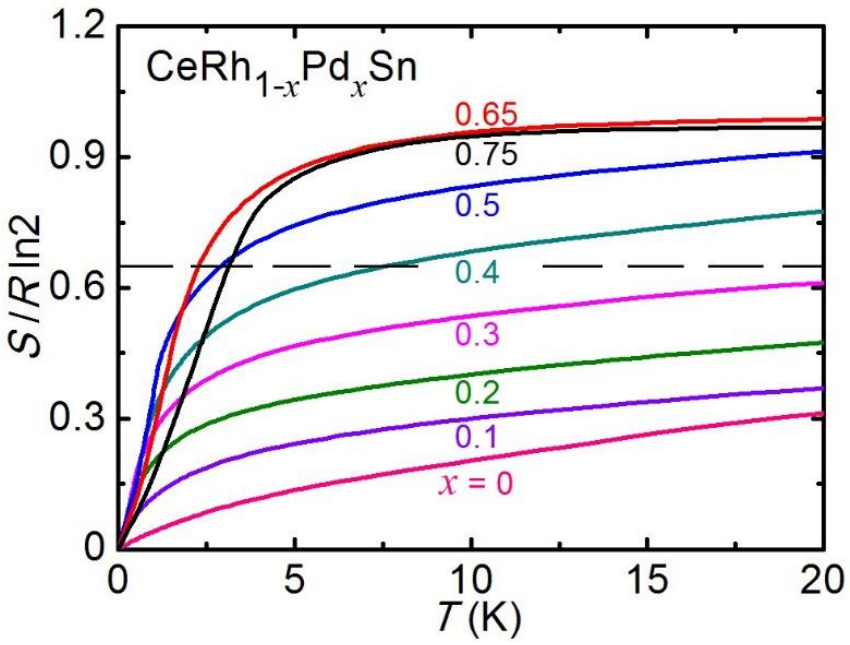

Figure 4.6: Magnetic entropy of $CeRh_{1-x}Pd_xSn$ as a function of temperature. The dashed line represents the value of $0.65R\ln 2$.

Field dependence of ac susceptibility

Here, we recall that the field dependence of C/T measured at 0.07 K for the single crystal with $x = 0$ showed a peak at 3.6 T only when the external field was applied along the a axis [72]. It was inferred as the evidence for the spin-flop crossover in the frustrated state. In order to examine this proposition, we have measured field dependence of χ_{ac} in $B \parallel a$ and $B \parallel c$ at various constant temperatures. As shown in Fig. 4.7, $\chi_{ac}(B \parallel c)$ at 0.05 K has no anomaly, whereas $\chi_{ac}(B \parallel a)$ at 0.03 K exhibits a peak at 3.5 T, in agreement with the field dependence of C/T. With increasing temperature to 0.62 K, the peak broadens and seems to separate into two maxima, as observed in C/T. Our observations support the proposition of spin-flop crossover of frustrated Ce moments in the ground state [72].

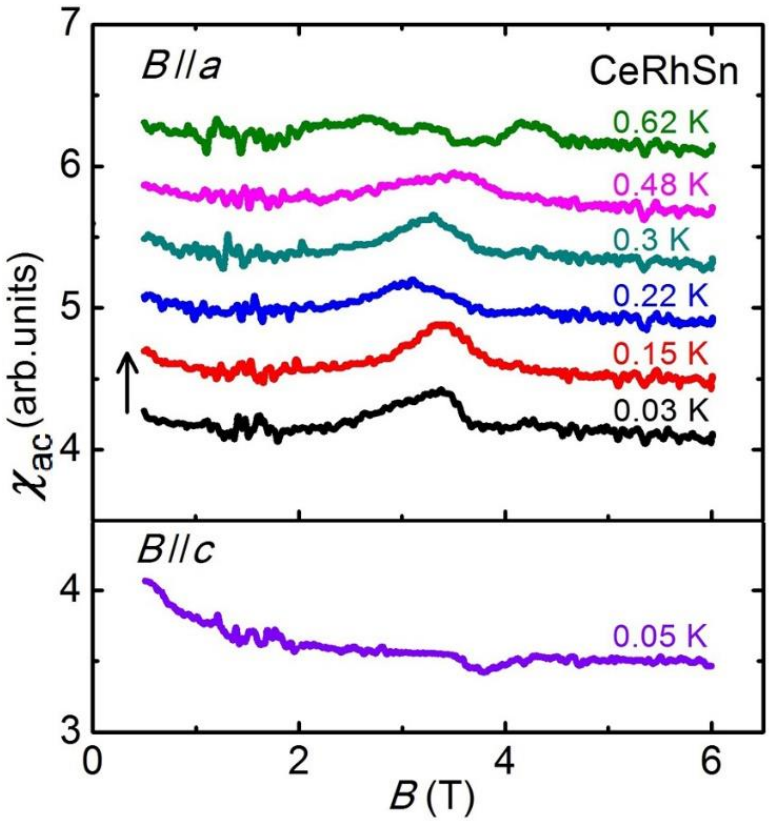

Figure 4.7: Isothermal ac susceptibility of the CeRhSn single crystal as a function of magnetic field B applied parallel to the a and c axes, respectively. The data are vertically shifted for clarity.

Resistivity, susceptibility, and magnetoresistance of single crystals $CeRh_{1-x}Pd_xSn$ (x = 0 and 0.1)

The ground state properties for x = 0 and x = 0.1 have been further studied by the measurements of $\rho(T)$, $\chi(T)$, and magnetoresistance (MR) on single crystals. Figure 4.8 shows $\rho(T)$ for the current directions $I \parallel a$ and $I \parallel c$. The data for x = 0 exhibit large anisotropy $\rho_a(T) > \rho_c(T)$ and a maximum in $\rho_a(T)$ at around 70 K. The successive decrease in $\rho_a(T)$ on cooling is a characteristic of a Ce-based Kondo compound in the coherent scattering regime. For x = 0.1, the large anisotropy is maintained, but the maximum in $\rho_a(T)$ is absent, as seen in the inset where the magnetic part is replotted vs ln$T$. The continuous increase in $\rho_a(T)$ down to 0.04 K is attributed to the loss of coherence in the quasikagome Kondo lattice by atomic disorder. The weak upturn in both $\rho_a(T)$ and $\rho_c(T)$ at temperatures below 20 K is similar to that observed in the polycrystalline sample with x = 0.2 in Fig. 4.3.

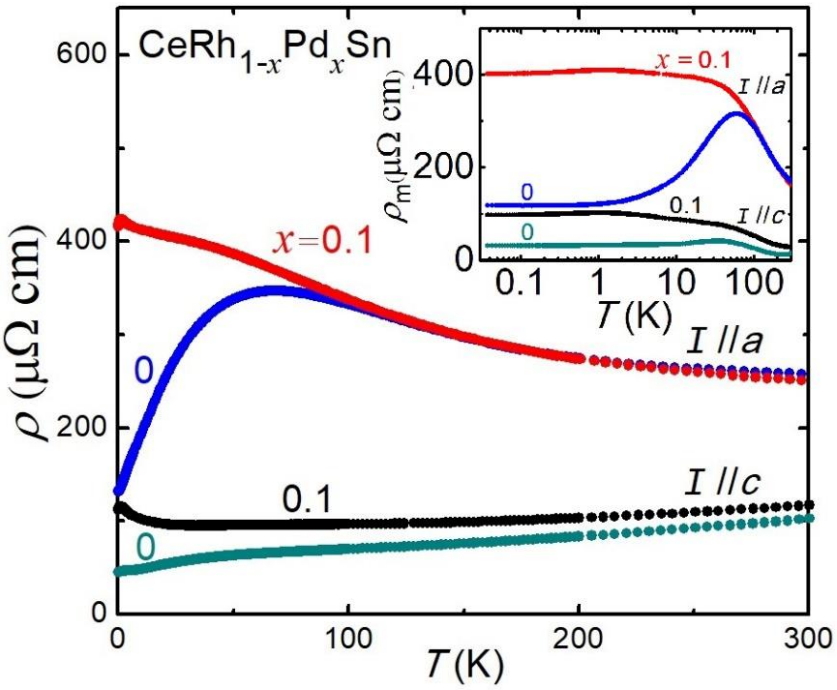

Figure 4.8: Electrical resistivity of single crystals $CeRh_{1-x}Pd_xSn$ with x = 0 and 0.1 for the current I parallel to the a and c axes, respectively. The inset shows the magnetic contribution to the resistivity ρ_m vs log$T$.

Figure 4.9 represents a double logarithmic plot of dc susceptibility $\chi(T)$ for single crystals with $x = 0$ and 0.1 in a field of 0.1 T applied || a and || c. The large anisotropy $\chi_c(T) >> \chi_a(T)$ is maintained for $x = 0.1$, which is similar for $x = 0$ [68]. In the temperature range 0.8–5 K, $\chi_c(T)$ and $\chi_a(T)$ for $x = 0$ follow the power law $\chi(T) \propto T^{-n}$ with $n = 1.1$ and 0.35, respectively [68]. The values of n for $x = 0.1$ converge to 0.6 for both $\chi_c(T)$ and $\chi_a(T)$. As shown in the inset, $M(B \parallel c)$ at 0.3 K reaches a value of 0.32 μ_B/f.u., being four times larger than that of $M(B \parallel a)$. The magnitude of $M(B \parallel a)$ for $x = 0.1$ is comparable with that of $M(B \parallel c)$ for $x = 0$.

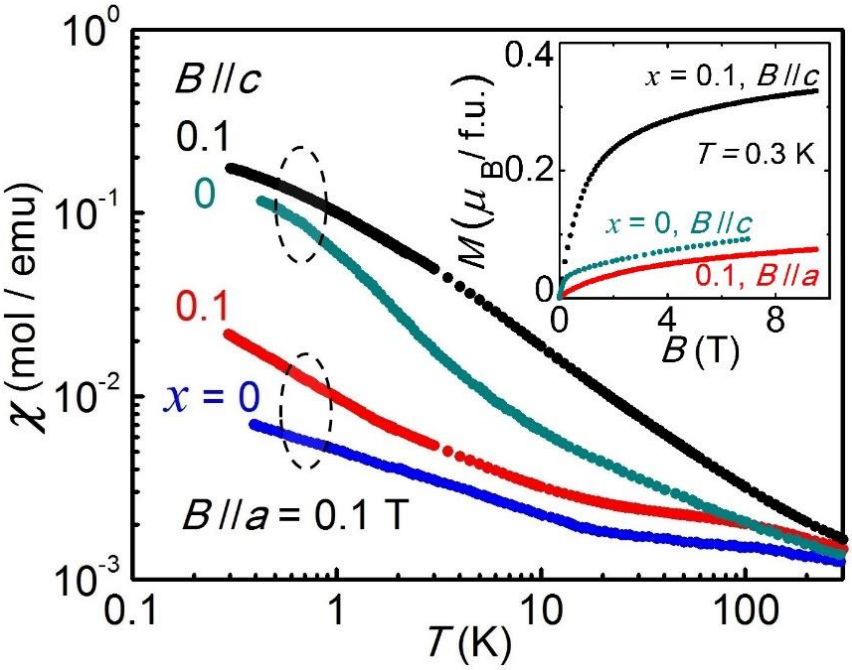

Figure 4.9: dc magnetic susceptibility of single crystals of $CeRh_{1-x}Pd_xSn$ with $x = 0$ and 0.1 for $B \parallel a$ and $B \parallel c$, respectively. The inset shows the isothermal magnetization for $B \parallel a$ and $B \parallel c$ at 0.3 K. The data for $x = 0$ are derived from ref. [68].

The MR was measured at various constant temperatures. Figure 4.10 represents the relative MR, $\{\rho(B) - \rho(B = 0)\}/\rho(B = 0)$, measured at the lowest temperature 0.08 K for the configurations $B \parallel I$ and $B \perp I$. For $x = 0$, MRs in the four configurations are all positive. The fact that the values of MR ($I \parallel a$, $B \parallel c$) and MR ($I \parallel c$, $B \parallel c$) are comparable is an indication for the positive MRs not being originated from cyclotron motions of conduction electrons because cyclotron motions occur only under $B \perp I$. A positive MR for $B \parallel I$ is expected to appear for a Ce-based heavy fermion system with a gap-like structure above the Fermi level [94]. It is actually observed for a valence-fluctuating compound $CePd_3$ [95] and a heavy fermion compound $CeRu_2Si_2$ [96]. Therefore, the observed positive MR for $x = 0$ is likely to be the characteristic of the gap-like structure in coherent Kondo lattice compounds. The change in the slope of MR at around $B \parallel a = 4$ T may be originated from the spin-flop crossover that appeared in the field dependence of C/T and χ_{ac}. On the contrary, MRs for $x = 0.1$ are all negative as shown in Fig. 4.10(b). The absolute value of MR for $I \parallel B \parallel c$ at 8 T is approximately five times larger than that for $I \parallel B \parallel a$, in which relation is similar with that of $M(B \parallel c) \cong 5M(B \parallel a)$ as shown in the inset of Fig. 4.9. This correlation between the MR and magnetization indicates that the negative MR is caused by the field-induced suppression of impurity Kondo scattering [97]. We also measured $\rho(T)$ under various constant magnetic fields shown in Fig. 4. 11 and found that the negative MR for $B \parallel c$ becomes significant at $T < 10$ K. In this temperature range, $\rho(T)$ for both $I \parallel a$ and $I \parallel c$ turns up on cooling as shown in Fig. 4.8.

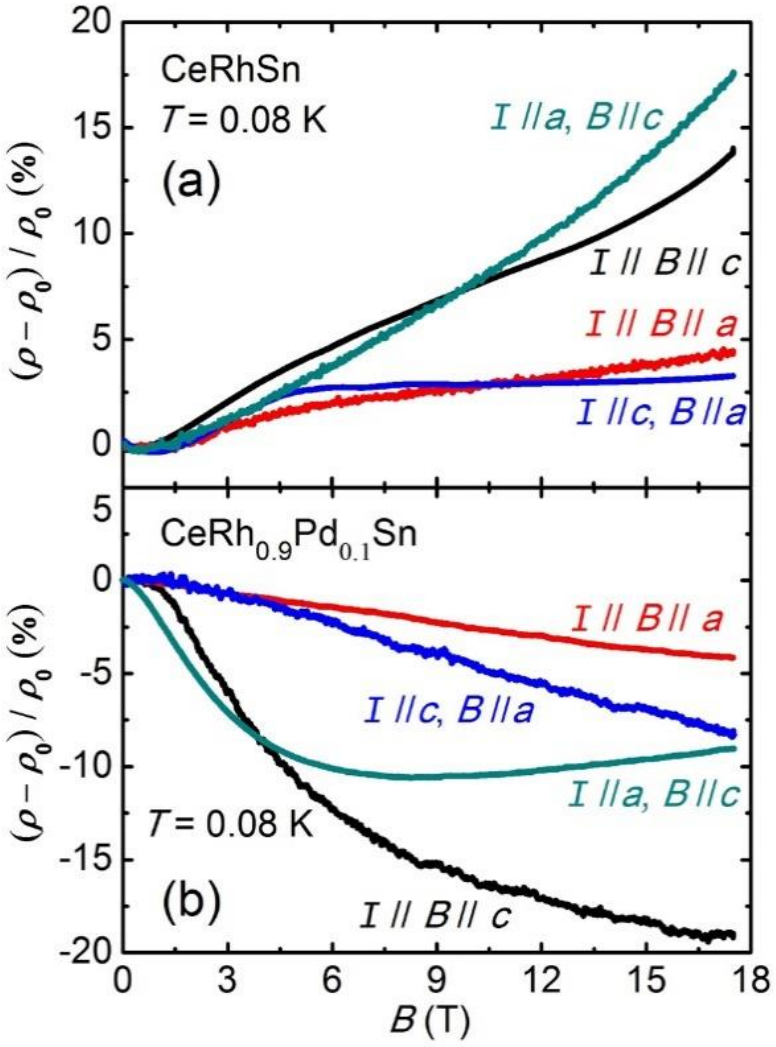

Figure 4.10: Normalized magnetoresistance for single crystals $CeRh_{1-x}Pd_xSn$ with $x = 0$ (a) and $x = 0.1$ (b) at 0.08 K in the applied fields $B \parallel a$ and $B \parallel c$ for the longitudinal ($B \parallel I$) and transverse ($B \perp I$) configurations.

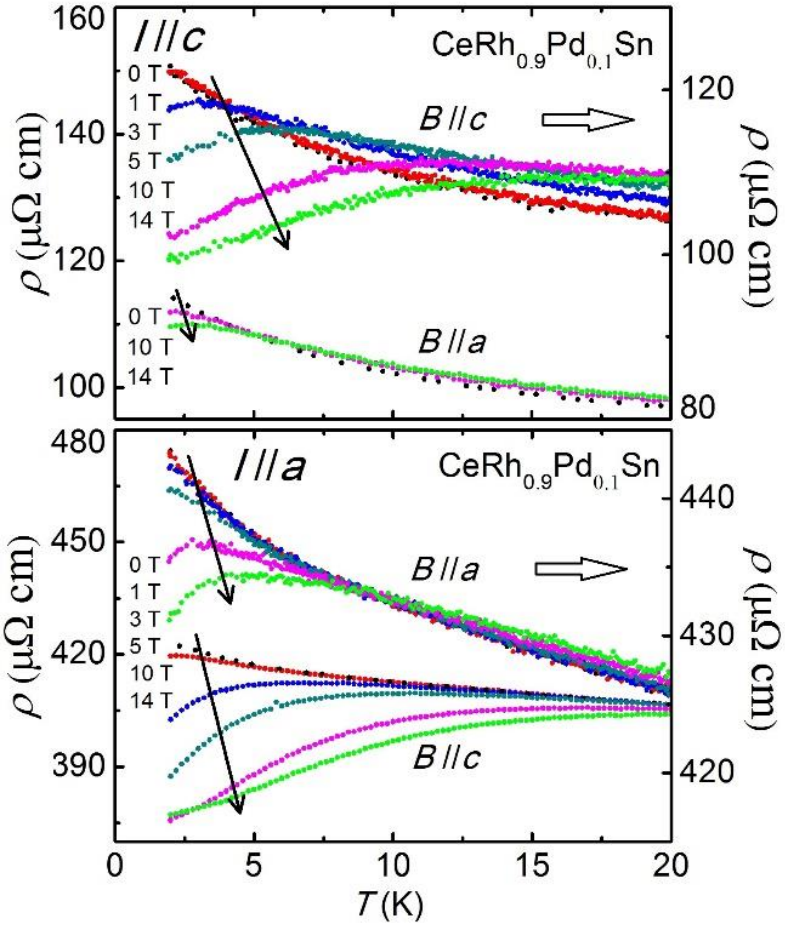

Figure 4.11: Electrical resistance for the single crystal $CeRh_{0.9}Pd_{0.1}Sn$ in the applied fields $B \parallel a$ and $B \parallel c$ for the longitudinal ($B \parallel I$) and transverse ($B \perp I$) configurations.

4.2 Transport, magnetic, and thermal properties of $CePd_3Sn_2$

We have studied the transport, magnetic, and thermal properties of $CePd_3Sn_2$ by the measurements of $\rho(T)$, $\chi(T)$, $M(B)$, and $C(T)$ for polycrystalline samples of $CePd_3Sn_2$ and its nonmagnetic reference $LaPd_3Sn_2$.

Electrical resistivity

Figure 4.12 shows $\rho(T)$ of $CePd_3Sn_2$ plotted vs log$T$ from 0.04 K up to 300 K. The value at 300 K is 67 $\mu\Omega$ cm, about 1/3 of the values reported for $CePd_3Al_2$ and $CePd_3In_2$ [79, 80]. On cooling, $\rho(T)$ gradually decreases without showing strong anomaly. The low-temperature data below 3 K is shown in the inset of Fig. 4.12. An obvious drop appears in $\rho(T)$ at 0.6 K, which gives rise to a peak in the slope dρ/dT, indicating a phase transition. In order to estimate the magnetic contribution ρ_m, $\rho(T)$ of $LaPd_3Sn_2$ was measured down to 2 K. The data were fitted by the modified Bloch-Gruneisen-Mott model [98] and extrapolated to 0.04 K, as shown in Fig. 4.12. At low temperatures, we see no sign of Kondo scattering in $\rho_m(T)$, in contrast with $CePd_3In_2$, where $-\ln T$ dependence of $\rho(T)$ was observed from 15 K to 3 K. It was attributed to the Kondo scattering of conduction electrons by the 4f electrons in the doublet CEF ground state [80].

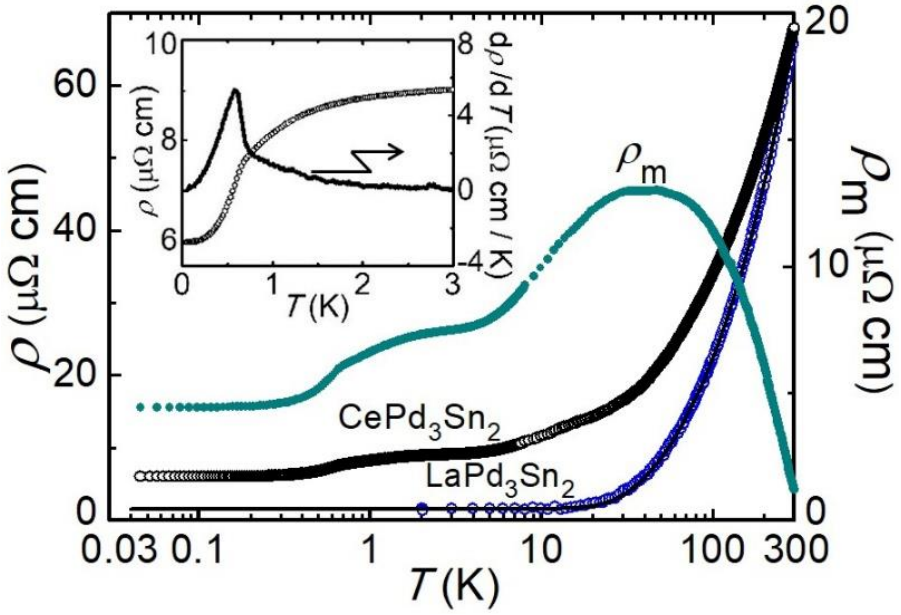

Figure 4.12: Temperature dependence of electrical resistivity of $CePd_3Sn_2$ and $LaPd_3Sn_2$. The magnetic contribution ρ_m is the difference between them. The inset shows the low-temperature data of $\rho(T)$ and the slope dρ/dT for $CePd_3Sn_2$.

Magnetic susceptibility and magnetization

The temperature dependence of inverse susceptibility is plotted in Fig. 4.13. The solid line above 80 K represents the fit by the modified Curie-Weiss formula $(\chi - \chi_0)^{-1} = (T - \theta_p)/C$, where θ_p is the paramagnetic Curie temperature and χ_0 is the temperature independent contribution, 1.0×10^{-4} emu/mol. The obtained effective moment $\mu_{eff} = 2.44\ \mu_B$ is close to the value expected for a free Ce^{+3} ion and the negative valve of $\theta_p = -8$ K suggests the AFM interaction among the magnetic moments. The left inset shows the low-temperature χ vs T, where the maximum at 0.6 K suggests an AFM order. In the right inset, the isothermal magnetization at 0.5 K bends at around 4 T and reaches 1.2 μ_B/Ce at 10 T. This magnitude is comparable with the value of 1.0 μ_B/Ce reported for $CePd_3Al_2$ under a similar condition [79].

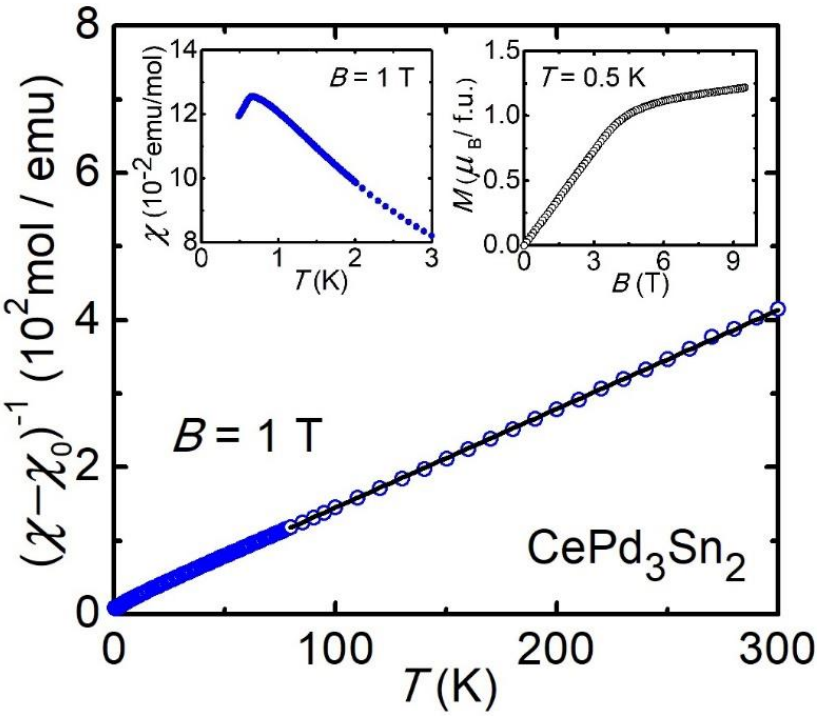

Figure 4.13: Temperature dependence of the inverse magnetic susceptibility for $CePd_3Sn_2$. The solid line represents the modified Cure-Weiss fit. Left inset: low-temperature magnetic susceptibility below 3 K. Right inset: isothermal magnetization as a function of magnetic field at 0.5 K.

Specific heat

The overall temperature dependence of specific heat for $CePd_3Sn_2$ is plotted in the inset of Fig. 4.14. The low-temperature data exhibits a sharp peak at 0.6 K, which temperature agrees with that of the peaks in $d\rho/dT$ (inset of Fig. 4.12) and $\chi(T)$ (left inset of Fig. 4.13). It is worth noting that $C(T)$ has a remarkable tail from 0.6 K up to 3 K. Because the Kondo effect is not observed in $\rho_m(T)$, we intend to analyze the tail in $C(T)$ in terms of AFM short-range correlations. The dashed curve represents the fit to the data with the specific heat of $S = 1/2$ uniform AF chain calculated by Klümper [75, 76]. The fit with the exchange interaction $J/k_B = 1.8$ K is rather good between 1.0 and 2.0 K. The experimental data at $T > 2$ K exceed the fit, which is attributed to the tail of the Schottky amomaly of crystal field excitaions as described below. In order to obtain the magnetic entropy S_m, C/T data of $LaPd_3Sn_2$ and $CePd_3Sn_2$ were extrapolated to $T = 0$ with the equations $C/T = \gamma + \beta T^2$ and $C/T = \gamma + \beta T^2 + \delta T^2 e^{-\Delta/k_B T}$, respectively, which are relevant for a nonmagnetic metal and an antiferromagnet having spin wave excitations with an anisotropic gap Δ [99]. The fit for $LaPd_3Sn_2$ revealed the Sommerfeld coefficient $\gamma = 2.7$ mJ/K^2 mol and the Debye coefficient $\beta = 1.08$ mJ/K^{4}mol (Debye temperature $\Theta_D = 220$ K). The fit using the value of β for $CePd_3Sn_2$ led to the γ value of 240 mJ/K^2 mol, which can be attributed to quantum fluctuations one-dimensional AF chains [77]. The AF magnon gap $\Delta = 1.1$ K is comparable with T_N.

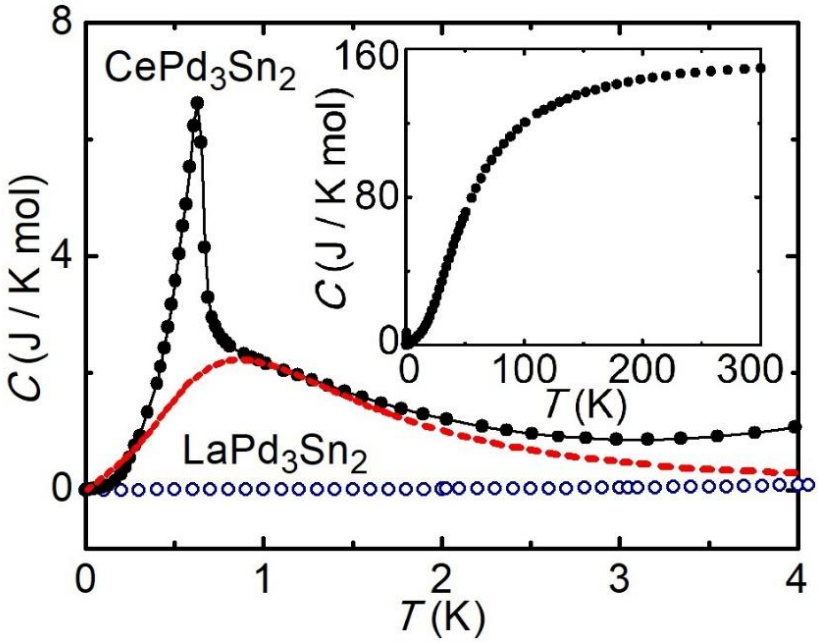

Figure 4.14: Low-temperature specific heat of $CePd_3Sn_2$ and $LaPd_3Sn_2$ below 4 K. The dashed red curve represents the theoretical specific heat of an $S = 1/2$ AFM uniform Heisenberg chain with $J/k_B = 1.8$ K [76, 77]. The inset shows the overall data for $CePd_3Sn_2$.

Magnetic entropy

As shown in Fig. 4.15, S_m reaches 0.42Rln2 at T_N = 0.6 K and reaches Rln2 at around 4 K. In view of the lack of Kondo contribution in $\rho(T)$ below 3 K, the pronounced tail in the specific heat $C(T)$ between 0.6 and 3 K is associated with the AFM short-range correlations in the one-dimensional Ce-Ce chains. In the inset of Fig. 4.15, $C_m(T)$ exhibits two Schottky anomalies peaking at 12 and 100 K, respectively. The values of S_m reach 0.94Rln4 and 0.91Rln6 at temperature above the Schottky anomalies. The relation for energies of CEF excited doublets $\Delta_{CEF} = T_{Cmax}/0.416$ gives the values of Δ_{CEF} as 29 K and 240 K, respectively. The presence of two excited doublets is consistent with the CEF level scheme expected for the orthorhombic symmetry of the Ce^{3+} ion.

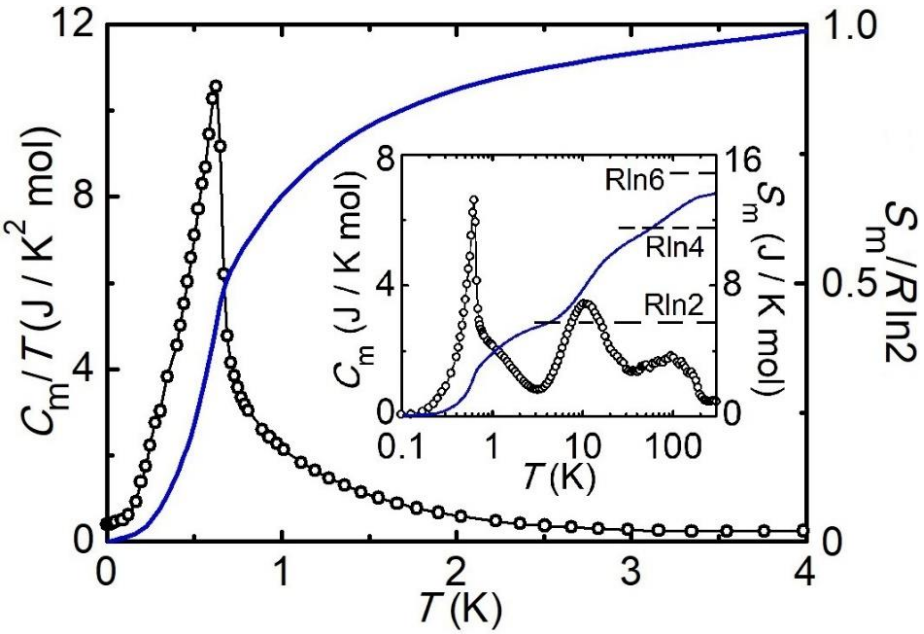

Figure 4.15: Magnetic specific heat $C_m = C(CePd_3Sn_2) - C(LaPd_3Sn_2)$ divided by temperature and magnetic entropy S_m of $CePd_3Sn_2$ below 4 K. The inset shows $C_m(T)$ and $S_m(T)$ up to 300 K.

In order to obtain more detailed information of the CEF excitations and relevant energy levels, the inelastic neutron scattering (INS) experiments on polycrystalline samples of $CePd_3Sn_2$ and $LaPd_3Sn_2$ were performed using the time-off-flight chopper spectrometer MERLIN at the ISIS pulsed neutron and muon facility, UK. Figures. 4.16 and 4.17 show the Q-averaged one-dimensional energy cuts at 5 K from 12 and 38 meV incident energies, respectively. Two apparent peaks of INS excitation for $CePd_3Sn_2$ are observed at 2.3 meV (27 K) and 16.5 meV (191 K), which are absent in the nonmagnetic reference compound $LaPd_3Sn_2$. The results agree with the values of Δ_{CEF} obtained from the $C_m(T)$, which confirms the presence of two excited CEF doublets above the ground state of the Ce^{3+} ion.

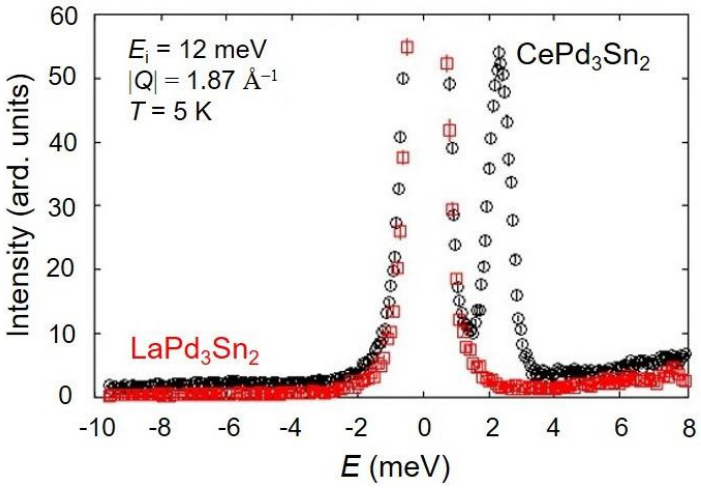

Figure 4.16. Inelastic neutron scattering intensity vs transfer energy of $CePd_3Sn_2$ and $LaPd_3Sn_2$ at |Q| = 1.87 Å measured with E_i = 12 meV at 5 K.

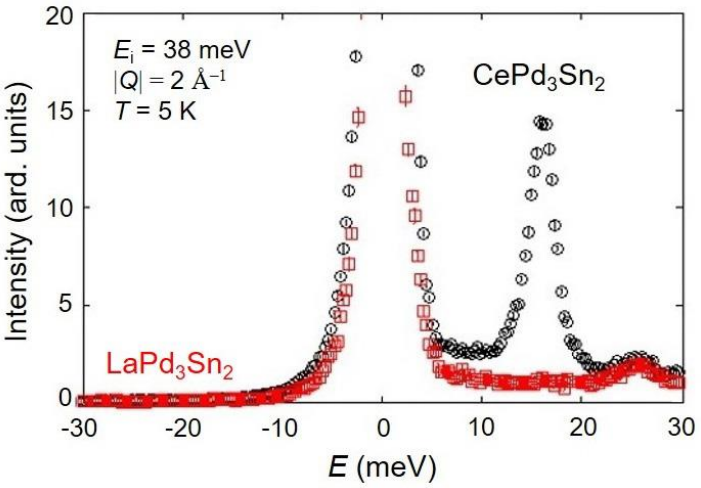

Figure 4.17. Inelastic neutron scattering intensity vs transfer energy of $CePd_3Sn_2$ and $LaPd_3Sn_2$ at |Q| = 2 Å measured with E_i = 38 meV at 5 K.

Chapter 5

Summary

$CeRh_{1-x}Pd_xSn$

Magnetic frustration in the quasikagome lattice of Ce atoms in the *c*-plane of CeRhSn has been expected to place this compound near the quantum critical point. In order to confirm this expectation and to study how the ground state changes in $CeRh_{1-x}Pd_xSn$, we have measured the magnetic, transport, and thermal properties at temperatures down to 0.03 K. It is found that χ_{ac} for $x = 0$ shows a broad maximum at 0.1 K, whereas $C(B \parallel a)/T$ keeps increasing down to 0.07 K. Upon applying magnetic fields along the *a* axis, $\chi_{ac}(B)$ at 0.03 K exhibits a peak at 3.5 T, which is consistent with the peak observed in C/T at 3.6 T. The metamagnetic behavior in the field applied along the hard axis is attributed to destruction of magnetic frustration among Ce moments in the quasikagome plane. This confirms that the frustration hinders the long-range magnetic order in CeRhSn. The maximum in ρ(T) due to coherent scattering disappears for $x \geq 0.1$ and both C/T and $\chi_{ac}(T)$ exhibit a maximum, whose temperature increases from 0.1 K for $x = 0.1$ to 2.5 K for $x = 0.75$. Thereby, the magnetic entropy at 20 K increases from $0.36R\ln 2$ to $0.96R\ln 2$, indicating the full recovery of the magnetic freedom of the doublet ground state. It is naively conjectured that the quantum effect on the frustration is weakened in a fully localized moment state of $J = 5/2$ than in a reduced moment state for $x < 0.1$. We infer that the appearance of magnetic order in $CeRh_{1-x}Pd_xSn$ for $x \geq 0.1$ is the consequence of suppressions of the Kondo effect and magnetic frustration. The role of frustration in the phase diagram needs to be further studied by microscopic experiments such as neutron scattering and NMR. All our observations corroborate that the ground state of the quasikagome Kondo lattice CeRhSn is very close to the QCP resulting from the interplay among Kondo effect, RKKY interaction, and geometrical frustration.

$CePd_3Sn_2$

X-ray single crystal analysis of a new Ce-based ternary compound $CePd_3Sn_2$ showed that it crystalizes in the orthorhombic structure of the $CePd_3In_2$-type with Ce-Ce chains along the *b* axis. A long-range AFM order at T_N = 0.6 K manifests itself as the characteristic anomalies in the electrical resistivity, magnetic susceptibility, and specific heat. The temperature dependence of the magnetic specific heat suggested the the presence of excited CEF doublets at 29 K and 240 K above the ground doublet, which agrees with those directly obtained by neutron scattering experiments. The extended tail in $C(T)$ and the upward curvature in $\rho(T)$ at $T > T_N$ are attributed to the AFM short-range correlations in one dimensional Ce-Ce chains along *b* axis. The effects of short-range correlations on physical properties need to be studied using single crystalline samples.

Acknowledgements

This work involves my three years of study at the Experimental Magnetism Laboratory, Graduate School of Advanced Sciences of Matter, Hiroshima University. I sincerely thank to the Professors and students who helped me to conduct the PhD work during three years. I am deeply attracted to the rigorous attitude on research and active academic environment here. I realize that obtaining excellent scientific achievements need devote all myself to the research and insist on it for enough time.

First of all, I express my personal respect and gratitude to my academic supervisor Prof. T. Takabatake. Since the first meeting at Zhejiang Univ. in 2015, I have been motivated by his earnest attitude to scientific research and gracious encouragement to students. Due to his suggestion and recommendation, I got more opportunities to extend my experience on advanced facilities at NIMS and ISIS to obtain important data for my thesis. Without his teaching and help, I couldn't insist on completing it. In addition, I really appreciate the patient instructions on measurements and reasonable advises from Profs. K. Umeo, T. Onimaru, K. Suekuni, and Y. Shimura. Furthermore, I am grateful to the collaborations with Drs. N. Kikugawa, T. Terashima, and S. Uji of Research Center for Functional Materials, NIMS and D. T. Adroja of ISIS facility, UK. The low-temperature data of ac susceptibility and magnetoresistance and the results of inelastic neutron scattering provided me with the direct evidences for the quantum criticality in quasikagome lattice $CeRh_{1-x}Pd_xSn$ and the CEF level scheme in $CePd_3Sn_2$, respectively.

Secondly, I should thank J. Kawabata, K. Hayashi, Y. Yamane, D. Watanabe, and S. Tsuda from at the Experimental Magnetism Laboratory for the assistances on experiments and useful discussions. They took their breaks to help me with no strings attached. I also appreciate the help from all the Japanese students during the activities outside the laboratory, which made my life rich and varied in Japan.

Finally, I should thank for my motherland. Her prosperity and strength gave me a chance to study in Japan. I express my gratitude to my wife and parents. They are strong emotional and financial supporters to make me complete my PhD work.

Bibliography

[1] J. Jensen and A. R. Mackintosh, *Rare Earth Magnetism Structures and Excitations* (Clarendon Press, Oxford, 1991).

[2] P. Misra, *Heavy-Fermion Systems* (Elsevier, Amsterdam, 2008).

[3] A.C. Hewson, *The Kondo Problem to Heavy Fermions* (Cambridge University Press, Cambridge, 1993).

[4] P. Coleman, *Introduction to Many-Body Physics*, (Cambridge University Press, Cambridge, 2015).

[5] M. Vojta, Phys. Rev. B **78**, 125109 (2008).

[6] P. Coleman and A. H. Nevidomskyy, J. Low Temp. Phys. **161**, 182 (2010).

[7] Q. Si, J. H. Pixley, E. Nica, S. J. Yamamoto, P. Goswami, R. Yu, and S. Kirchner, J. Phys. Soc. Jpn. **83**, 061005 (2014).

[8] S. Blundell, *Magnetism in Condensed Matter*, (Oxford University Press, New York, 2001).

[9] A. H. Wilson, *The theory of metals*, (Cambridge University Press, Cambridge, 1953).

[10] N. E. Alekseevakii and Yu. P. Gaidukow, Soviet Physics **4**, 807 (1957).

[11] J. Kondo, Prog. Theor. Phys. **32**, 37 (1964).

[12] J. Kondo, Solid State Phys. **23**, 183 (1969).

[13] T. Kasuya, Prog. Theor. Phys. **16**, 45 (1956).

[14] M. A. Ruderman and C. Kittel, Phys. Rev. **96**. 99 (1954).

[15] K. Yosida, Phys. Rev. **106**, 893 (1957).

[16] S. Doniach, Physica B **91,** 231 (1977).

[17] B. Coqblin, *The Electronic Structure of Rare-Earth Metal and Alloys: The Magnetic Heavy Rare-Earths* (Academic Press, London, 1977).

[18] P. A. Lee, T. M. Rice, J. W. Serene, L. J. Sham, and J. W. Wilkins, Comments Cond. Matter Phys. **12**, 99 (1986).

[19] G. R. Stewart, Rev. Mod. Phys. **56**, 755 (1984).

[20] K. Kadowaki and S. B. Woods, Solid State Commun. **58**, 507 (1986).

[21] M. T. Beal-Monod, Physica B **109&110**, 1837 (1982).

[22] G. E. Brodale, R. A. Fischer, Norman E. Phillips, G. R. Stewart, and A. L. Giorgi, Phys. Rev. Lett. **57**, 234 (1986).

[23] C. L. Seaman, M. B. Maple, B. W. Lee, S. Ghamaty, M. S. Torikachvili, J. S. Kang, L. Z. Liu, J. W. Allen, and D. L. Cox, Phys. Rev. Lett. **67**, 2882 (1991).

[24] C. Lacroix, P. Mendeles, and F. Mika, (Eds.) *Introduction to Frustrated Magnetism*: *Materials, Experiments, Theory*, (Springer, New York, 2011).

[25] L. Balents, Nature (London) **464**, 199 (2010).

[26] C. Lacroix, J. Phys. Soc. Jpn. **79**, 011008 (2010).

[27] B. H. Bernhard, B. Coqblin, and C. Lacroix, Phys. Rev. B **83**, 24427 (2011).

[28] S. Julian and H. -Y. Kee, Physics in Canada **68**, 95 (2012).

[29] K. Takada, H. Sakurai, E. Takayama-Muromachi, F. Izumi, R. A. Dilanian and T. Sasaki, Nature **422**, 53 (2003).

[30] H. Urayama, H. Yamochi, G. Saito, K. Nozawa, T. Sugano, M. Kinoshita, S. Sato, K. Oshima, A. Kawamoto, and J. Tanaka, Chem. Lett. **17**, 55 (1988).

[31] E. Wawrzynska, R. Coldea, E. M. Wheeler, I. I. Mazin, M. D. Johannes, T. Sörgel, M. Jansen, R. M. Ibberson, and P. G. Radaelli, Phys. Rev. Lett. **99**, 157204 (2007).

[32] H. Yoshida, Y. Muraoka, T. Sörgel, M. Jansen, and Z. Hiroi, Phys. Rev. B **73**, 020408 (2006).

[33] H. Yoshida, S. Ahlert, M. Jansen, Y. Okamoto, J. I. Yamaura, and Z. Hiroi, J. Phys. Soc. Jpn. **77**, 074719 (2008).

[34] S. Ishiwata, D. Wang, T. Saito, and M. Takano, Chem. Matter. **17**, 2789 (2005).

[35] Y. Uchida, Y. Kanke, E. Takayama-Muromachi, and K. Kato, J. Phys. Soc. Jpn. **60**, 2530 (1991).

[36] D. I. Gorbunov, M. S. Henriques, A. V. Andreev, Y. Skourski, and M. Dusek, J. Alloys Compd. **634**, 115 (2015).

[37] D. I. Gorbunov, T. Nomura, I. Ishii, M. S. Henriques, A. V. Andreev, M. Doerr, T. Stöter, T. Suzuki, S. Zherlitsyn, and J. Wosnitza, Phys. Rev. B **97**, 184412 (2018).

[38] F. Iga, A. Shigekawa, Y. Hasegawa, S. Michimura, T. Takabatake, S. Yoshii, T. Yamamoto, M. Hagiwara, and K. Kindo, J. Mag. Mag. Mat. **310**, e443 (2007).

[39] L. Ye, T. Suzuki, and J. G. Chechelsky, Phys. Rev. B **95**, 174405 (2017).

[40] S. Yoshii, T. Yamamoto, M. Hagiwara, S. Michimura, A. Shigekawa, F. Iga, T. Takabatake, and K. Kindo, Phys. Rev. Lett. **101**, 087202 (2008).

[41] M. S. Kim, M. C. Bennett, and M. C. Aronson, Phys. Rev. B **77**, 144425 (2008).

[42] S. Nakatsuji, Y. Machida, Y. Maeno, T. Tayama, T. Sakakibara, J. van Duijn, L. Balicas, J. N. Millican, R. T. Macaluso, and J. Y. Chan, Phys. Rev. Lett. **96**, 087204 (2006).

[43] Y. Taguchi, Y. Oohara, H. Yoshizawa, N. Nagaosa, and Y. Tokura, Science **291**, 2573 (2001).

[44] S. Kondo, D. C. Johnston, C. A. Swenson, F. Borsa, A. V. Mahajan, L. L. Miller, T. Gu, A. I. Goldman, M. B. Maple, D. A. Gajewski, E. J. Freeman, N. R. Dilley, R. P. Dickey, J. Merrin, K. Kojima, G. M. Luke, Y. J. Uemura, O. Chmaissem, and J. D. Jorgensen, Phys. Rev. Lett. **78**, 3729 (1997).

[45] M. Shiga, K. Fujisawa, and H. Wada, J. Phys. Soc. Jpn. **62**, 1329 (1993).

[46] S. Yonezawa, Y. Muraoka, and Z. Hiroi, J. Phys. Soc. Jpn. **73**, 1655 (2004).

[47] A. Dönni, G. Ehlers, H. Maletta, P. Fischer, H. Kitazawa, and M. Zolliker, J. Phys.: Condens. Matter **8**, 11213 (1996).

[48] A. Oyamada, S. Maegawa, M. Nishiyama, H. Kitazawa, and Y. Isikawa, Phys. Rev. B **77**, 064432 (2008).

[49] V. Fritsch, N. Bagrets, G. Goll, W. Kittler, M. J. Wolf, K. Grube, C. L. Huang, and H. v. Löhneysen, Phys. Rev. B **89**, 054416 (2014).

[50] V. Fritsch, O. Stockert, C.-L. Huang, N. Bagrets, W. Kittler, C. Taubenheim, B. Pilawa, S. Woitschach, Z. Huesges, S. Lucas, A. Schneidewind, K. Grube, and H. v. Löhneysen, Eur. Phys. J. Spec. Top. **224**, 997 (2015).

[51] A. Sakai, S. Luchas, P. Gegenwart, O. Stockert, H. v. Löhneysen, V. Fritsch, Phys. Rev. B **94**, 220405(R) (2016).

[52] Y. Isikawa, T. Kuwai, T. Mizushima, T. Abe, G. Nakamura, and J. Sakurai, Physica B **281**, 365 (2000).

[53] V. Fritsch, C. L. Huang, N. Bagrets, K. Grube, S. Schumann, and H. v. Löhneysen, Phys. Status Solidi B **250**, 506 (2013).

[54] E. Brück, H. Nakotte, K. Bakker, F. R. de Boer, P. F. de Châtel, J.-Y. Li, J. P. Kuang, and F.-M. Yang, J. Alloys Compd. **200**, 79 (1993).

[55] B. Gibson, R. Pöttgen, R. K. Kremer, A. Simon and K. R. A. Ziebeck, J. Alloys Compd. **239**, 34 (1996).

[56] F. Merlo, M. Pani, and M. L. Fornashini, J. Alloys Compd. **232**, 289 (1996).

[57] K. Katoh, Y. Mano, K. Nakano, G. Terui, Y. Niide, and A. Ochiai, J. Magn. Magn. Mater. **268**, 212 (2004).

[58] K. Umeo, K. Yamane, Y. Muro, K. Katoh, Y. Niide, A. Ochiai, T. Morie, T. Sakakibara, and T. Takabatake, J. Phys. Soc. Jpn. **73**, 537 (2004).

[59] H. Kubo, K. Umeo, K. Katoh, A. Ochiai, and T. Takabatake, J. Phys. Soc. Jpn. **77**, 023704

(2008).

[60] A. Oyamada, K. Kamioka, K. Hashi, S. Maegawa, T. Goto, and H. Kitzawa, J. Phys. Soc. Jpn. **65** Suppl. B, 123 (1996).

[61] F. Hulliger, J. Alloys Compd. **196**, 225 (1993).

[62] H. Kitazawa, A. Matsushita, T. Matsumoto, and T. Suzuki, Physica B **199-200**, 28 (1994).

[63] T. Goto, S. Hane, K. Umeo, T. Takabatake, and Y. Isikawa, J. Phys. Chem. Solids **63**, 1159 (2002).

[64] H. C. Zhao, J. H. Zhang, S. L. Hu, Y. Isikawa, J. L. Luo, F. Steglich, and P. J. Sun, Phys. Rev. B **94**, 235131 (2016).

[65] S. Lucas, K. Grube, C.-L. Huang, A. Sakai, W. Wunderlich, E. L. Green, J. Wosnitza, V. Fritsche, P. Gegenwart, O Stokert, and H. v. Löhneysen, Phys. Rev. Lett. **118**, 107204 (2017).

[66] R. Mishra, R. Pöttgen, R, -D. Hoffman, H. Trill, B. D. Mosel, H. Piotrowski, and M. F. Zumdick, Z. Naturforsch. **56b**, 589 (2001).

[67] A. Ślebarski, M. B. Maple, E. J. Freeman, C. Sirvent, M. Radlowska, A. Jezuerski, E. Granado, Q. Huang, and J. W. Lynn, Phil. Mag. B **82**, 943 (2002).

[68] M. S. Kim, Y. Echizen, K. Umeo, S. Kobayashi, M. Sera, P. S. Salamakha, O. L. Sologub, and T. Takabatake, Phys. Rev. B **68**, 054416 (2003).

[69] H. Higaki, I. Ishii, D. Hirata, M. S. Kim, T. Takabatake, and T. Suzuki, J. Phys. Soc. Jpn. **75**, 024709 (2006).

[70] S. F. Matar, J. F. Riecken, B. Chevalier, R. Pöttgen, A. F. Al Alam, and V. Eyert, Phys. Rev. B **76**, 174434 (2007).

[71] A. Schenck, F. N. Gygax, M. S. Kim, and T. Takabatake, J. Phys. Soc. Jpn. **73**, 3099 (2004).

[72] Y. Tokiwa, C. Stingl, M. S. Kim, T. Takabatake, and P. Gegenwart, Sci. Adv. **1**, e1500001 (2015).

[73] L. Havela, M. Diviš, V. Sechovský, A. V. Andreev, F. Honda, G. Oomi, Y. Méresse, and S. Heathman, J. Alloys Compd. **322**, 7 (2001).

[74] H. Hegger, C. Petrovic, E. G. Moshopoulou, M. F. Hundley, J. L. Sarrao, Z. Fisk, and J. D. Thompson, Phys. Rev. Lett. **84,** 21 (2000).

[75] Z. Hossain, T. Takabatake, C. Geibel, P. Gegenwart, I. Oguro, and F. Steglich, J. Phys.: Condens. Matter **13**, 4535 (2001).

[76] A. Klümper, Eur. Phys. J. **B5**, 677 (1998).

[77] D. C. Johnston, R. K. Kremer, M. Troyer, X. Wang, A. Klümper, S. L. Bud'ko, A. F.

Panchula, and P. C. Canfield, Phys. Rev. B **61**, 9558 (2000).

[78] S. N. Nesterenko, A. I. Tursina, P. Rogl, and Y. D. Seropegin, J. Alloys Compd. **373** 220 (2004).

[79] E. Khamitcaeva, A. Tursina, A. Gribanov, D. Gnida, P. Wisniewski, and D. Kaczorowski, J. Alloys Compd. **708,** 162 (2017).

[80] H. Kaldarar, E. Royanian, H. Michor, G. Hilscher, E. Bauer, A. Gribanov, D.Shtepa, P. Rogl, A. Grytsiv, Y. Seropegin, and S. Nesterenko, Phys. Rev. B. **79** 205104 (2009).

[81] O. Niehaus, P. M. Abdala, and R, Pöttgen, Z. Naturforsch. **70**, 253 (2015).

[82] G. M. Sheldrick, SHELXL-97 Program for crystal structure refinement, (University of Göttingen, Germany, 1997); McArdle, Windows version OSCAIL, (Natl. Univ. Ireland, Galway, 1997); G. M. Sheldrick, Acta Crystallogr. **A64**, 112-122 (2008).

[83] T. Sakakibara, H. Mitamura, T. Tayama, and H. Amitsuka, J. Appl. Phys. **33**, 5067 (1994).

[84] Quantum Design, San Diego, CA 92121-1311, *QuantumDesign* PPMS Heat Capacity Option User's Manual (2009).

[85] M. Gamza, A. Slebarski, and H. Resner, Eur. Phys. J. B **67**, 483 (2009).

[86] D. Gignoux and J. C. Gomez-Sal, Phys. Rev. B **30**, 3967 (1984).

[87] W. P. Beyermann, M. F. Hundley, P. C. Canfield, J. D. Thompson, M. Latroche, C. Godart, M. Selsane, Z. Fisk, and J. L. Smith, Phys. Rev. B **43**, 13130 (1991).

[88] K. Barros, J. W. F. Venderbos, G. W. Chen, and C. D. Batista, Phys. Rev. B **90**, 245119 (2014).

[89] H. Ishizuka and Y. Motome, Phys. Rev. B **91**, 085110 (2015).

[90] S. Ghosh, P. O'. Brien, C. L. Henley, and M. Lawler, Phys. Rev. B **93**, 024401 (2016).

[91] M. B. Brodsky, Rep. Prog. Phys. **41**, 1547 (1978).

[92] B. R. Cooper, Proc. Phys. Soc. **80**, 1225 (1962).

[93] H.-U Desgranges and K. D. Schotte, Phys. Lett. A **91**, 240 (1982).

[94] N. Kawakami and A. Okiji, J. Phys. Soc. Jpn. **55**, 2114 (1986).

[95] M. Houshiar, D. T. Adroja, and B.D. Rainford, Physica B **223-224**, 268 (1996).

[96] S. Kambe, H. Suderow, J. Flouquet, P. Haen, and P. Lejay, Solid State Commun. **95**, 449 (1995).

[97] P. Schlottman, Z. Phys. B **51**, 223 (1983).

[98] S. Baran, D. Kaczorowski, A. Arulraj, B. Penc, and A. Szytuła, J. Magn. Magn. Mater. **322**, 2177 (2010).

[99] B. R. Cooper, Proc. Phys. Soc. **80**, 1225 (1962).

Articles

(1) Quantum criticality and development of antiferromagnetic order in the quasikagome Kondo lattice $CeRh_{1-x}Pd_xSn$,
C. L. Yang, S. Tsuda, K. Umeo, Y. Yamane, T. Onimaru, T. Takabatake, N. Kikugawa, T. Terashima, and S. Uji,
Physical Review B **96**, 045139 /1-7 (2017).

(2) Evolution of a magnetic order in the quasikagome lattice system $CeRh_{1-x}Pd_xSn$ ($x \leq 0.75$),
C. L. Yang, K. Umeo, and T. Takabatake,
Journal of Physics: Conference Series **807**, 042001 /1-6 (2017).

(3) Structural and magnetic properties of a novel ternary intermetallic compound $CePd_3Sn_2$,
C. L. Yang, S. Tsuda, K. Umeo, T. Onimaru, W. Paschinger, G. Giester, P. Rogl, and T. Takabatake,
Journal of Alloys and Compounds **739**, 518-521 (2018).

Thesis Supplements

(1) Effects of W substitution on the magnetic properties, phase evolution and microstructure of rapidly quenched $Co_{80}Zr_{18}B_2$ alloy,
Z. P. Hou, C. L. Yang, S. F. Xu, J. B. Zhang, D. Liu, F. Su, and W. Q. Wang,
Journal of Magnetism and Magnetic Materials **368**, 116-120 (2014).

(2) Kondo effect in the quasiskutterudite $Yb_3Os_4Ge_{13}$,
C. L. Yang**,** X. Wang, X. Zhang, D. S. Wu, M. Liu, P. Zheng, J. Y. Yao, Z. Z. Li, Y.-F. Yang, Y. G. Shi, J. L. Luo, and N. L. Wang,
Physical Review B **91**, 075120 /1-7 (2015).

(3) Evidence for half-metallicity in *n*-type $HgCr_2Se_4$,
T. Guan, C. J. Lin, C. L. Yang, Y. G. Shi, C. Ren, Y. Q. Li, H. M. Weng, X. Dai, Z. Fang, S. S. Yan, and P. Xiong,
Physical Review Letters **115**, 087002 /1-6 (2015).

(4) Superconductivity emerging from a suppressed large magnetoresistant state in tungsten ditelluride,
D. F. Kang, Y. Z. Zhou, W. Yi, C. L. Yang, J. Guo, Y. G. Shi, S. Zhang, Z. Wang, C. Zhang, S. Jiang, A. G. Li, K. Yang, Q. Wu, G. M. Zhang, L. L. Sun, and Z. X. Zhao,
Nature Communications **6**, 7804 /1-6 (2015).

(5) Quantum oscillations, thermoelectric coefficients, and the Fermi surface of semimetallic WTe_2,
Z. W. Zhu, X. Lin, J. Liu, B. Fauqué, Q. Tao, C. L. Yang, Y. G. Shi, and K. Behnia,
Physical Review Letters **114**, 176601 /1-5 (2015).

(6) Raman scattering investigation of large positive magnetoresistance material WTe_2,
W. D. Kong, S. F. Wu, P. Richard, C. S. Lian, J. T. Wang, C. L. Yang, Y. G. Shi, and H. Ding,
Applied Physics Letters **106**, 081906 /1-4 (2015).

(7) Large and anisotropic linear magnetoresistance in bulk stoichiometric Cd_3As_2 crystals,
D. S. Wu, X. Wang, X. Zhang, C. L. Yang, P. Zheng, P. G. Li, and Y. G. Shi,
Science China Physics, Mechanics and Astronomy **58**, 017501 /1-6 (2015).

(8) Effect of hydrostatic pressure on the superconducting properties of quasi-1D superconductor $K_2Cr_3As_3$,
J. P. Sun, Y. Y. Jiao, C. L. Yang, W. Wu, C. J. Yi, B. S. Wang, Y. G. Shi, J. L. Luo, Y. Uwatoko, and J. G. Cheng,
Journal of Physics: Condensed Matter **29**, 455603 /1-7 (2017).